

TOPICAL REVIEW

Nanocrystals for silicon-based light-emitting and memory devices

S K Ray^{1,3}, S Maikap², W Banerjee² and S Das¹

¹ Department of Physics and Meteorology, Indian Institute of Technology, Kharagpur-721302, India

² Thin Film Nano Tech. Lab., Department of Electronic Engineering, Chang Gung University, Tao-Yuan, Taiwan 333, Taiwan

E-mail: physkr@phy.iitkgp.ernet.in

Received 22 October 2012, in final form 18 February 2013

Published 22 March 2013

Online at stacks.iop.org/JPhysD/46/153001

Abstract

Nanocrystals (NCs), representing a zero-dimensional system, are an ideal platform for exploring quantum phenomena on the nanoscale, and are expected to play a major role in future electronic and photonic devices. Here we review recent progress in the growth, characterization and utilization of some group-IV semiconductors (Si and Ge), metal and high- k NCs for silicon planar technology compatible light-emitting and floating gate memory devices. We first introduce the size-dependent electrical and optical properties of Si and Ge NCs. We outline some of the schemes to achieve light emission from indirect band gap Si and Ge NCs embedded in different high band gap oxide matrices. In particular, special emphasis is given on the review of the advances in Ge NCs because of some of their intriguing electronic and optical properties. We then describe the use of semiconductor and metal NCs as floating gates for non-volatile memory devices to achieve high data retention and faster program/erase speeds. The exploitation of high- k oxides with tunable and variable injection barriers for improved charge storage devices is discussed. Finally, the integration of single and multilayer metallic NCs and multilayer high- k oxides as floating gates is explored by the fabrication and testing of memory transistors.

(Some figures may appear in colour only in the online journal)

1. Introduction

Low-dimensional structures, known as nanostructures, exhibit superior properties as compared with their bulk counterpart making them attractive for functional applications. Nanocrystals (NCs) or quantum dots (with size less than the excitonic Bohr radius), also known as a zero-dimensional system, representing a novel form of crystalline materials have drawn enormous interest due to their superior optical [1–5] and electronic [6–10] properties. Semiconductor NCs, in particular, provide means to create artificial potentials for electrons and holes with tunable barriers, offering an ideal platform for experimental realization of quantum effects in low-dimensional systems. Moore's law has been used as the benchmark for aggressive scaling of devices to achieve ever

increasing performance. However, the integration of photonic components with the mature silicon CMOS technology is required in the near future to maintain the progress in high-speed computing and communication. A major bottleneck in the integration of optoelectronics and microelectronics is the lack of Si-compatible light sources.

Different approaches have been made to achieve light emission from group-IV semiconductor heterostructures [11, 12] and nanostructures [1, 3, 4, 13–18]. Light emission using the conversion of group-IV semiconductors from the indirect band gap to a quasi-direct one through Brillouin zone folding and other approaches has been extensively reviewed [19]. Photoluminescence [20, 21] and electroluminescence (EL) [22] of Si/SiGe superlattices have been reported by many research groups [20–22]. The observation of strong visible photoluminescence from porous silicon at room temperature

³ Author to whom any correspondence should be addressed.

[23] in 1990 stimulated substantial activity in the field of silicon nanostructures for optical sources. The study of group-IV semiconductor NCs has been motivated by the prediction that quantum confinement (QC) of carriers may lead to efficient luminescence despite the indirect nature of the energy gaps. This has led to several research studies on light emission in the visible wavelength range from nanocrystalline silicon/Ge films [24] and Si [1, 4, 25–28] and Ge [14, 16, 29–31] NCs embedded in an SiO_2 matrix. A number of contradictory results have also shown the influence of defect states in the NCs or in the NC–oxide interface [32, 33] on the observed photon emission, keeping the field wide open for further investigation. One of the alternative approaches, resulting in emission in the mid-infrared and THz, is through intersubband transitions [34, 35] in quantized energy levels, such as those occurring in quantum cascade lasers [36]. The development of silicon-based light sources with emission near the telecommunication wavelength ($1.54 \mu\text{m}$) has also been reported using the spin–orbit split $^4\text{I}_{13/2} \rightarrow ^4\text{I}_{15/2}$ transition of Er^{3+} -doped NCs in an oxide host matrix [37–41].

In addition to the enhancement of optical characteristics, QC and Coulomb blockade phenomena observed in semiconductor NCs allow their applications in Si-based nanoelectronic devices, namely single electron transistors [42–44] and quantum-dot floating gate memories (FGMs) [31, 45–47]. The use of a floating gate composed of isolated metal [48–54] or semiconductor [31, 45–47, 55–58] NCs reduces the extent of charge loss occurring in conventional flash memories, allowing for thinner tunnelling oxides (TOs) and, hence, smaller operating voltages, enhanced endurance, and faster write/erase speeds. The metallic NCs have been found to be very attractive in this regard because of the higher surface electric field, deeper quantum wells for charge storage and ease of fabricating multilayer NCs embedded in tunable barrier high-permittivity oxides that are used in Si memory technology.

This review focuses on the progress of silicon-based light-emitting and FGM devices using Si and Ge NCs embedded in oxide matrices. The optical properties of Stranski–Krastanov (SK) grown self-assembled Ge quantum dots, which have been dealt with in some excellent review papers [59–61], are not included here. Similarly, the light-emitting properties of compound semiconductor NCs are beyond the scope of this review, because of their direct band gap nature. On the other hand, the electrical properties of the metal and high- k NCs are discussed because of their compatibility with Si CMOS technology making them useful in future memory applications.

2. Band gap of Si and Ge NCs: effect of QC

One way to increase the oscillator strength of optical transitions in an indirect band gap semiconductor is through QC, resulting in a stronger overlap of electron–hole wave functions. QC modifies the free particle dispersion relation as a function of a system’s spatial dimension. The optical properties of quantum-confined systems are quite different from their bulk counterparts. The origin of photoluminescence from Si and Ge NCs has been attributed to excitonic emission in a quantum-confined system [14, 16, 25, 29]. Excitonic Bohr radius is

a useful stricture to study the QC in semiconductor NCs. When a hole is localized at the lattice site and a detached electron remains in its neighbourhood, they will be under the Coulombic interaction and can become bound to form a hydrogen-like atom. The resulting excitons have slightly less energy than the unbound electron and hole. The excitonic Bohr radius (a_B) of a material is expressed as

$$a_B = \frac{\hbar^2 \varepsilon}{\pi e^2} \left[\frac{1}{m_e^*} + \frac{1}{m_h^*} \right], \quad (1)$$

where ε is the permittivity of the material, m_e^* and m_h^* are the effective mass of electron and hole, respectively, and \hbar is the Planck constant. When the size of a semiconductor nanoparticle approaches its excitonic Bohr radius, the QC plays a dominant role. For example, the excitonic Bohr radii of GaAs [62], Si [63] and Ge [14] are estimated to be 14.7 nm, 4.9 nm and 24.3 nm, respectively, a dimension achievable using nanolithography in a top-down approach or through self-assembled growth via bottom-up methodology. An analytical model reported by Brus in 1986, predicting the QC effect in NCs, is given as [64]

$$E = E_g + \frac{\hbar^2}{8R^2} \left[\frac{1}{m_e^*} + \frac{1}{m_h^*} \right] - \frac{1.8e^2}{4\pi\varepsilon_0\varepsilon_\alpha R} - \frac{0.124e^4}{\hbar^2(4\pi\varepsilon_0\varepsilon_\alpha)^2} [1/m_e^* + 1/m_h^*]^{-1}, \quad (2)$$

where E is the onset of absorption of the sample, E_g is the bulk band gap, R is the radius of the particle, ε_0 is the vacuum permittivity and ε_α is the high-frequency dielectric constant of the semiconductor. The second term on the right-hand side of equation (2) is consistent with the quantum theory of a particle confined in a box, which is strongly size dependent and that explains the origin of the blueshift of the emission energy in NCs. On the other hand, the third term accounting for the Coulombic interaction between an electron and a hole lowers the energy and is relatively weakly size dependent. The effect of the fourth term on the quantum confined energy level is negligible.

Figures 1(a) and (b) present the reported theoretical [65–70] along with experimental results [18, 71–75] on the variation of band gap as a function of the size of Si and Ge NCs, respectively. The computations made by several research groups using time-dependent local density approximation (TDLDA) [67], effective mass approximation [65], tight binding (TB) [68, 69], empirical pseudo-potentials [70] methods are presented. In the effective mass theory approach, the effect of the periodic field in a crystal can be replaced by an effective electron (hole) mass tensor m^* . Based on the Luttinger and Kohn generalization of the effective mass approximation, Takagahara and Takeda [65] developed a model to calculate the electronic structure of silicon and germanium quantum dots. Garoufalidis *et al* [66] calculated the optical gap of small silicon quantum dots (figure 1(a)), with diameters up to 25 Å using time-dependent density functional theory and multi-reference second-order perturbation theory. Tsolakidis and Martin [67] reported the calculation of the optical properties of hydrogen-passivated germanium and silicon NCs using time-dependent density functional theory

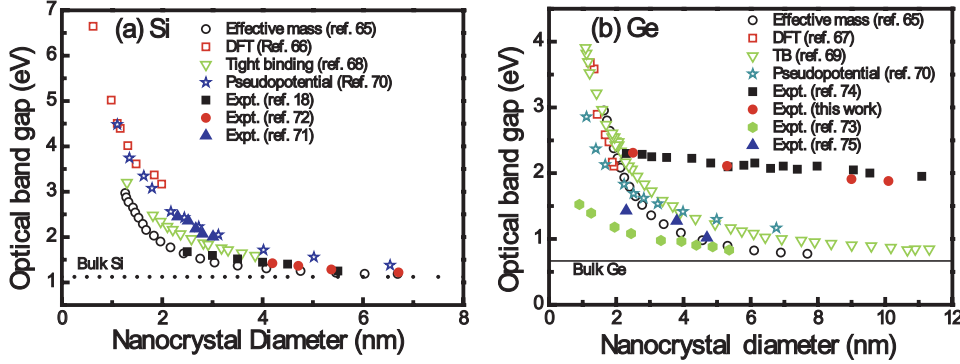


Figure 1. Reported theoretical (open symbol) along with experimental (filled up symbol) results on the variation of band gap as a function of diameter for (a) Si and (b) Ge NCs.

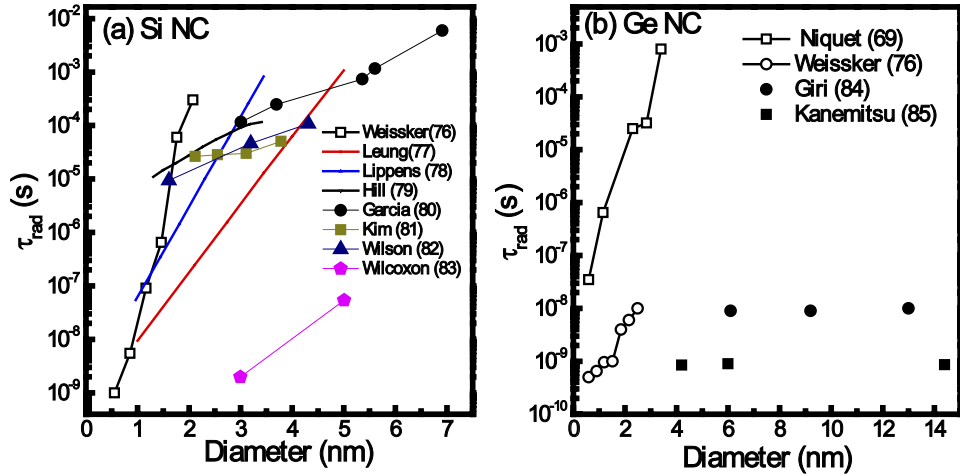


Figure 2. Variation of radiative lifetimes for (a) Si and (b) Ge NCs with diameter.

in the adiabatic local density approximation. Self-consistent methods such as the local density approximation can only be used for small clusters (<1000 atoms) with high symmetry. A semi-empirical method such as TB can solve much larger problems. Free exciton energy and lowest transition energy for Si NCs with a Si–O bond as a function of the cluster size were reported using the self-consistent TB method [68]. Niquet *et al* [69] fitted the energy of the highest valence state (E_v) and of the lowest conduction state (E_c) over the whole range of spherical Ge NC sizes using the TB method, as shown in figure 1(b). The pseudo-potential method has been used [70] to calculate the energy difference between the lowest unoccupied molecular orbital and the highest occupied molecular orbital (LUMO–HOMO). This method is often referred to as the exact band structure calculation, but the model requires a lot of empirical input. It is clear from figure 1 that the QC in Ge NC is larger than that of Si for the same size, as predicted from equation (2) because of the lighter carrier masses in Ge. From figure 1, it is evident that all the theoretical results closely follow the same trends for both Si and Ge NCs of increasing optical gap with decreasing NC size. It is difficult to make a quantitative comparison since most of these studies are semi-empirical in nature and usually rely on fitting parameters. The scarcity of optical data, particularly for Ge NCs, indicates the necessity of more experimental results for further understanding.

3. Size-dependent properties of Si and Ge NCs

The exciton binding energy in Si and Ge quantum dots plays an important role in exhibiting photoluminescence, which is predicted to be of excitonic origin even at room temperature. The estimated radiative lifetime of excitons is strongly size dependent and varies from nanoseconds to milliseconds corresponding to the crystallite size from ~ 1.0 to 3.0 nm. Weissker *et al* [76] calculated the radiative lifetime in Si and Ge NCs based on the independent-particle approximation at room temperature. Figures 2(a) and (b) present the theoretical [69, 76–79] lifetime data based on different semi-empirical treatments of the electronic structure along with the experimental results [74, 80–84] for Si and Ge NCs, respectively. As the quantum dot size is increased, the radiative decay rate decreases rapidly although the trend for Si and Ge is qualitatively different. In the crystallite size range 1.0 – 2.0 nm, the radiative lifetime of Si varies much more rapidly than that for Ge. This result is attributed to the remarkable differences in the oscillator strength of radiative transitions of Si and Ge NCs. In bulk Ge, the strong direct (E_0) transition occurs close to the indirect band gap, whereas in Si the E_0 transition and the indirect band gap are separated by about 2.5 eV. As a consequence, the radiative lifetime of Ge NCs is much shorter than that in Si crystallites. A comparison

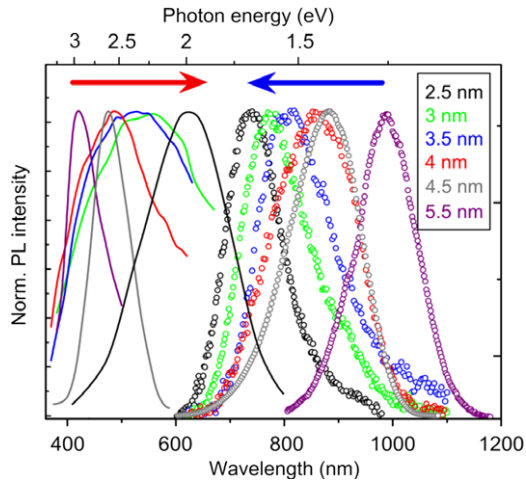


Figure 3. Size-dependent hot PL (with picosecond decay characteristics), and excitonic PL from Si NCs. The excitonic PL spectra show an expected QC effect while the hot PL peak exhibits a gradual redshift towards longer wavelength for smaller NCs. (Reprinted with permission from Macmillan Publishers Ltd: [18], copyright 2010).

of Si lifetime in terms of photo-luminescence energies rather than the diameter has been reported [65, 73, 85, 86]. The inhomogeneous size distribution in Si NCs and non-radiative recombination of excitons play crucial roles in controlling the photoluminescence decay dynamics. Thus, it is very important to investigate the radiative recombination and its dependence on the wavelength or the NC size, which can be utilized to identify the dominant luminescence mechanism. For Ge NCs, there are very few reported results on time decay measurements [74, 84, 87]. A decay time constant around 0.86 ns [74], which is found to be independent of the average Ge NCs size as well as the photon energy, has been reported. Decay dynamics of 1.2–3.2 nm Ge NCs has been reported [87]. The transition from indirect to direct recombination of carriers with decreasing size has resulted in very fast ($\ll 1 \mu\text{s}$) decay time for all the samples [87]. Recent reported results [88] show that the decay dynamics for Ge NCs embedded in Si is dominated by non-radiative recombination from the temperature- and energy-dependent PL decay measurements.

4. Optical emission characteristics of Si NCs

Luminescent Si NCs can be prepared by several techniques, such as silane decomposition in the gas phase [89], laser ablation [90], Si ion implantation at high doses in thermal oxide followed by a high-temperature annealing [91], sputtering [18, 71, 92] and chemical vapour deposition (CVD) [93, 94]. All the prepared Si NCs exhibit light emission at room temperature in the wavelength range 600–1100 nm. Excellent review articles on the EL and photoluminescence (PL) from Si NCs [95–98] are available in the literature. Boer *et al* [18] reported enhanced quantum efficiency in phonon-free photoluminescence from Si NCs. Figure 3 shows the reported size-dependent hot PL (with picosecond decay characteristics), and excitonic PL from Si NCs [18]. The excitonic PL spectra show an expected QC effect with blue shifted emission energy

for smaller sized NCs. On the other hand, the hot PL peak in the visible range exhibits a gradual redshift towards a longer wavelength for smaller NCs. The variation of the hot PL peak on NC size has been attributed to the radiative recombination in the NC core, rather than to defect states. The redshift of PL due to no-phonon radiative recombination in Si NCs has been explained theoretically [99]. The achievement of EL from NCs at a relatively low current injection is a necessary condition for their application in light-emitting devices (LEDs). Therefore, a right balance between good optical properties and electrical conduction of Si quantum dots is required. Wang *et al* [100] reported size-dependent EL in the wavelength range 550–800 nm from nanocrystalline Si. EL has also been demonstrated by embedding NCs in a metal–oxide–semiconductor field-effect transistor (MOSFET) device by sequential injection of carriers in the Si NCs gate [1]. Most of the reported silicon NC LEDs operate at a high bias voltage (>5 V) at which unipolar Fowler–Nordheim (F–N) tunnelling is the main charge injection mechanism [1, 17, 100]. In this case, hot electrons are responsible for the charge transport in the oxide, which leads to impact ionization in Si NCs resulting in the generation of electron–hole pairs. However, the fast degradation of the oxide matrix and resultant low device endurance are major concerns in the hot electron transport process, which may lead to the quenching of EL for Si NC LEDs [101]. On the other hand, direct or trap-assisted tunnelling (TAT) may dominate depending on the oxide thickness in stoichiometric oxide-based MOS LED devices [102]. EL measurements on the single layer Si NC LED show efficiencies below 1×10^{-3} [1, 17, 100, 101]. To improve the power efficiency, multilayer NCs with perfect order and controlled sizes have been employed, which could also reduce the required bias voltage. New approaches to synthesize size-controlled Si NCs have been reviewed [103]. They reported the synthesis of NCs between 2.0 and 20 nm, with the full-width at half-maximum (FWHM) of size distribution 1.0 nm, by introducing a superlattice structure into the device, as shown in figure 4(a). A phase separation process was employed, in which the annealing of the $\text{SiO}_x/\text{SiO}_2$ superlattices at higher temperatures (>900 °C) resulted in the formation of silicon clusters in an SiO_2 matrix. The size of the NCs could be controlled by the thickness of the SiO_x layer. Figure 4(b) shows the size-dependent photoluminescence spectra from a multilayer sample [103]. The observed PL intensity from this dense array of identical NCs was found to be around two orders of magnitude higher as compared with a single layer one with the same thickness [103]. Pavesi's group [98] demonstrated the bipolar current injection in thin nanocrystalline-Si/ SiO_2 multilayers. Figure 5 shows the reported [98] results on power efficiency as a function of injected current density for nanocrystalline-Si/ SiO_2 LEDs. They reported a maximum power efficiency of 0.17% at the smallest injected current density of $4.9 \times 10^{-4} \text{ mA cm}^{-2}$, where the optical power density is $1.4 \times 10^{-3} \mu\text{W cm}^{-2}$ [98]. The high power efficiency is attributed to the radiative recombination of excitons formed by both electron and hole injection into silicon NCs via a direct tunnelling mechanism.

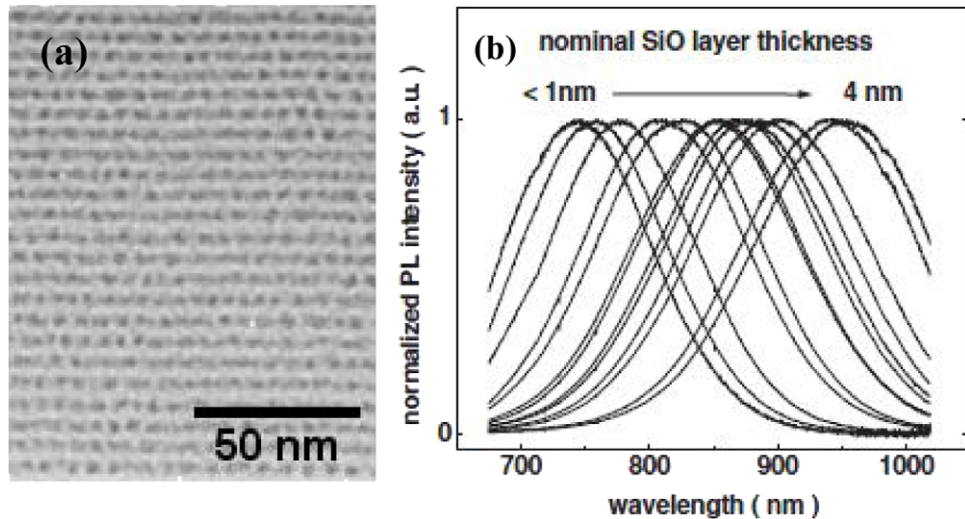


Figure 4. (a) Cross-sectional TEM image of the NC Si/SiO₂ superlattice in the crystallized state after annealing at 1100 °C. (b) Photoluminescence spectra of a set of superlattices with crystal sizes between 2 and 4 nm (layer thickness of 1–4 nm). (Reprinted with permission from Wiley-VCH Verlag GmbH & Co.: [103], copyright 2005).

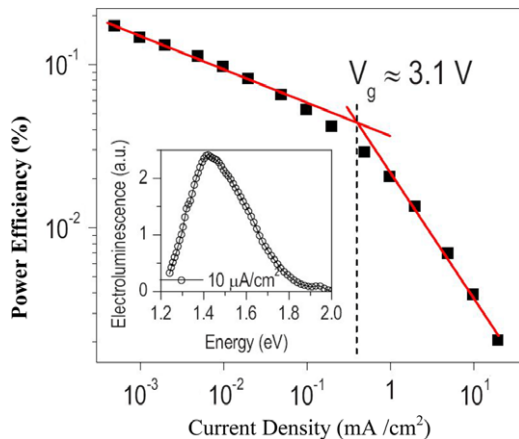


Figure 5. Power efficiency as a function of the injected current density for the multilayer Si NC LED. The inset shows the recorded EL spectrum for an injection current of 10 $\mu\text{A cm}^{-2}$. (Reprinted with permission from American Institute of Physics: [94], copyright 2009).

5. Properties of Ge NCs

As a group-IV element, Ge can be readily incorporated into silicon technologies. Ge is structurally similar to Si. The energy difference between the indirect gap (0.66 eV) and the direct gap (0.80 eV) is smaller in Ge ($\Delta E = 0.14$ eV) as compared with that of Si ($\Delta E = 2.28$ eV) Si. In comparison with Si, Ge has a larger dielectric permittivity and smaller effective masses for electrons and holes. Thus, the Bohr radius of the excitons in Ge (24.3 nm) [14] is larger as compared with that of Si (4.9 nm) [63]. The quantum size effect is thus predicted to be stronger in Ge than Si, as discussed previously in figure 1. Both of the above facts lead to an expectation that it is much easier to change the electronic structure around the band gap of Ge. The attainment of band-edge photoluminescence and energy quantized EL in Ge NCs is essential for the fabrication of NC LEDs. There

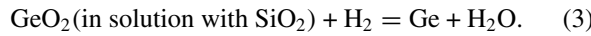
are only a few reports on Ge NC based electroluminescent devices due to the problematic carrier injection into NCs [104–107]. Using a high- k dielectric in place of SiO₂, a larger tunnelling current could be achieved in Ge NC based metal-insulator-semiconductor (MIS) LEDs due to the lower electron barrier height of Al₂O₃ or HfO₂ as compared with SiO₂ [107, 108]. Moreover, momentum conservation in a radiative process is facilitated by soft phonon scattering in high- k dielectrics [109]. This section represents a systematic study on the photoluminescence and EL characteristics from quantum confined Ge NCs embedded in different oxide matrices.

5.1. Growth of Ge NCs

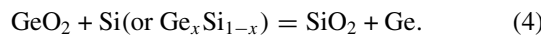
Several methods have been employed to synthesize Ge NCs in an oxide matrix, such as co-sputtering [14, 31, 110], CVD [29], ion implantation [33], pulsed laser deposition [107], sol-gel synthesis [41], and hydrothermal reduction of Si_xGe_{1-x}O₂ [30]. Ion implantation is one of the versatile techniques for forming Ge NCs in the near-surface region of a substrate. However, the disadvantage is that the NCs usually have a relatively wide size distribution. Multi-energy ion implantation and thermal annealing produce a uniform depth-concentration profile of Ge NCs over the SiO₂ film with a narrow size distribution. NCs are usually formed by implanting Ge with doses of $3 \times 10^{16} \text{ cm}^{-2}$ or higher at 100 keV and annealing at temperatures varying from 700 to 1000 °C. Oxidation of Ge due to the diffusion of oxidizing species from the annealing ambient at high temperatures plays an important role in samples with a projected range closer to the surface. Therefore, the structure of SiO₂ implanted with Ge and annealed thereafter is dependent on the processing parameters.

There has been a keen interest in the synthesis of Ge NCs in an oxide matrix via annealing of a co-sputtered oxide and Ge film. Maeda *et al* [14] reported the first observation of visible photoluminescence from Ge NCs embedded in a

SiO_2 glassy matrix prepared by radio frequency (rf) magnetron co-sputtering. The growth mechanism of Ge NCs involves the decomposition or reduction of GeO_2 into Ge. This decomposition or reduction takes place either in a forming gas ambient or even in a N_2 ambient in the presence of excess Si. Nitrogen in the forming gas ambient does not play any active role, while H_2 causes precipitation of Ge in the oxide matrix via the following reaction:



The Gibbs free energy of H_2 reduction in the above reaction is about -5 kJ mole^{-1} at 750°C . In addition, a mixed oxide state of Si and Ge, namely $\text{Ge}_x\text{Si}_{1-x}\text{O}_2$, in contact with unoxidized Si or $\text{Ge}_x\text{Si}_{1-x}$ is thermodynamically unstable. The germanium dioxide can be reduced to elemental Ge either by Si or $\text{Ge}_x\text{Si}_{1-x}$ due to the large negative free energy of the reaction



Experiment data of $\text{Ge}_x\text{Si}_{1-x}\text{O}_2$ film on a $\text{Ge}_x\text{Si}_{1-x}$ layer ($x = 0.28$ and 0.36), respectively, have shown that this reaction indeed occurs, but the process is limited kinetically to the close vicinity ($<10 \text{ nm}$) of the $\text{Ge}_x\text{Si}_{1-x}/\text{Ge}_x\text{Si}_{1-x}\text{O}_2$ interface, even after annealing at 900°C for 3 h [111]. The H_2 reduction of metastable $\text{Si}_{1-x}\text{Ge}_x\text{O}_2$ creates a sharper step profile as compared with the ion implantation technique, since the latter produces Gaussian-shaped NC density depth profiles. However, Ge NC formation via reduction of $\text{Si}_{1-x}\text{Ge}_x\text{O}_2$ is kinetically complex which, in turn, makes the prediction and control of size distribution difficult. It is interesting to note that the reduction of mixed oxide by Si produces Ge NCs in close proximity ($\sim 10 \text{ nm}$) to the oxide/substrate interface (not throughout the entire oxide), since the diffusivity of Si in oxide is quite small. This leads to a great advantage for applications in Ge NC memory devices, with a thin tunnel oxide for injection of electrons from the Si substrate, which will be discussed in section 9.1.

Transparent glass is a useful host matrix for Ge nanoparticles mainly for its application in optical fibre communication. The sol–gel method is an attractive route for glass preparation because it provides unusual compositions at a temperature much lower than that required in the conventional melt technique. Ge NCs embedded in silica containing 7.0 wt% Ge by the sol–gel method have been synthesized [112] using $\text{Si}(\text{OC}_2\text{H}_5)_4$ (TEOS) and GeCl_4 as starting materials to study the luminescence in the visible region. Gels synthesized by the hydrolysis of a complex solution of $\text{Si}(\text{OC}_2\text{H}_5)_4$ and $\text{Cl}_3\text{Ge}-\text{C}_2\text{H}_4-\text{COOH}$ followed by heating in H_2 gas atmosphere to form cubic Ge-NC embedded silica glasses have also been demonstrated [113]. The size of the NCs is strongly dependent on the annealing temperature and time in H_2 atmosphere [41]. Solution-based methods is a simple and robust way to produce macroscopic amount of Ge nanoparticles. Chemical methods are intriguing because of their potential use for hybrid solar cell and surface modification. Typical solution routes to Ge nanoparticles include chemical reaction of Ge Zintl salts [114], thermal

decomposition of metal-organic complexes in high-boiling solvents [115] or supercritical CO_2 [116], and chemical reduction of Ge salts using strong reducing agents such as alkali metals [117], n-butyl lithium [118], alkali metal naphthalides [119] and metal hydrides [120]. The effect of variables such as solvents, reducing agents, reaction temperature and capping ligands on the chemical synthesis of Ge NCs has been studied in detail [121].

5.2. Structural and vibrational properties of Ge NCs

The structural, mechanical, electronic and optical properties of NCs are very sensitive to the number of atoms contained therein. The size is expected to affect the amorphized content as well as the melting temperature, heat capacity and electronic properties of Ge NCs depending on their vibrational dynamics. The predicted interfacial amorphous layer between the crystalline core and oxide matrix acts as radiative and non-radiative recombination centres, which significantly affect the light emission characteristics of embedded Ge NCs. Growth and structural properties of SiO_2 -embedded Ge NCs have been studied extensively over the last two decades [16, 29–31, 47, 122].

5.2.1. Size of Ge NCs in different oxide matrices. Figure 6(a) shows the typical transmission electron micrograph (TEM) image of Ge NCs embedded in an SiO_2 matrix prepared by rf-sputtering of SiGe in an $\text{Ar}+\text{O}_2$ atmosphere and subsequent annealing at 900°C in N_2 ambient for 2 h [31]. The NCs are near-spherical shaped, which are dispersed in the amorphous SiO_2 matrix with diameter in the range 4–7 nm. The selected area electron diffraction pattern in figure 6(b) reveals that these NCs consist of cubic Ge in GeO_2 with tetragonal structure. Figure 6(c) shows a typical cross-sectional micrograph of the annealed Ge NC sandwiched between top and bottom oxides, which shows the formation of isolated spherical-shaped (27–32 nm) aligned Ge NCs about 30 nm away from the SiO_2/Si interface. It is well recognized that an as-prepared rf co-sputtered film of Ge and SiO_2 contains not only elemental Ge and oxides of Si, but also oxides of Ge [16, 31]. In such a Si–Ge–O ternary system, the direct decomposition of GeO_2 is the simplest reaction for the reduction of GeO_2 to Ge as given by



In fact, it has also been reported that Ge oxides in a Si–O–Ge system would be reduced to elemental Ge at elevated temperatures above 800°C [29].

These reduction reactions are as follows:



It has been suggested that the elemental Si originally existing in the matrix, due to the non-stoichiometric oxide, is insufficient for the reduction purpose. Instead, the largest supply of Si atoms for these reduction reactions originates from the Si substrate on which the film is deposited [30]. The driving force for the diffusion of Si atoms from the substrate and the

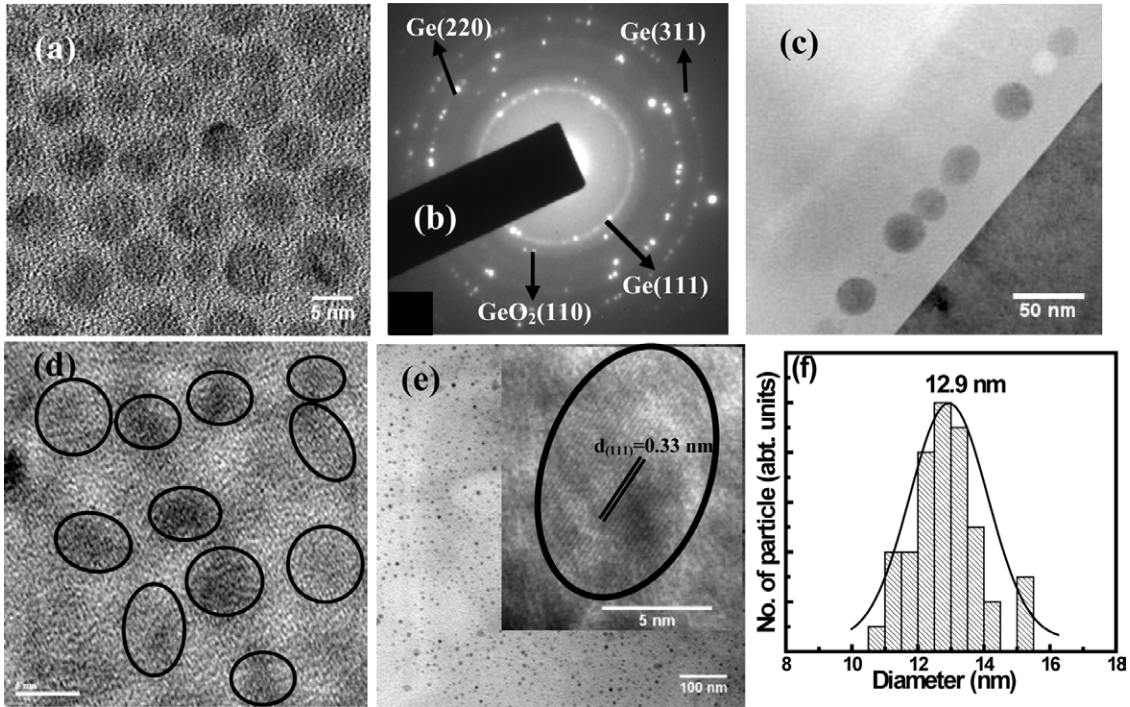


Figure 6. (a) Plane-view TEM micrographs of Ge NCs embedded in an SiO_2 matrix [31], (b) the selected area electron diffraction pattern reveals that these NCs consist of cubic Ge in GeO_2 with tetragonal structure. (c) Typical cross-sectional TEM micrograph showing aligned Ge NCs about 30 nm away from the SiO_2/Si interface. (d) Plane-view TEM micrograph of Ge NCs embedded in HfO_2 annealed at 800°C . (e) Plane-view TEM micrograph of Ge NCs embedded in an Al_2O_3 matrix for 950°C annealed temperature. The inset shows the lattice fringes of one such NC and (f) the size distribution of Ge NCs in the Al_2O_3 matrix.

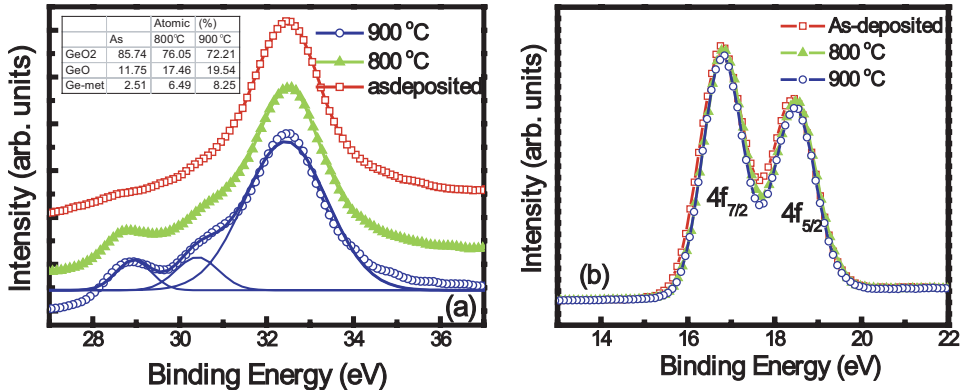


Figure 7. (a) Ge 3d and (b) Hf 4f XPS spectra for Ge NCs embedded in an HfO_2 matrix for as-deposited and annealed samples. The table in the inset of (a) shows the increase in metallic Ge with increasing annealing temperature.

precipitation of Ge atoms is attributed to the reduction in Gibbs free energy in these reactions.

In recent times, there have been numerous reports on the synthesis of Ge NCs in high- k dielectrics such as Al_2O_3 [123], Hf-based oxide [56, 85, 110] and SiON [111], as the low band gap high- k dielectric materials offer better carrier injection for NC LED and NC-based FGM devices. Figure 6(d) shows a typical plane-view TEM micrograph of the Ge NCs embedded in HfO_2 and annealed at 900°C in N_2 ambient. It shows the formation of Ge NCs with diameter 6–9 nm. Figure 7(e) shows the plane-view TEM image of Ge NCs embedded in an Al_2O_3 matrix annealed at 900°C . The dark patches seen are Ge NCs embedded in an amorphous Al_2O_3 matrix. The NCs are almost spherical and are well dispersed in the host matrix. The inset of figure 6(e) shows the lattice fringes, with

an inter-planar separation of 0.33 nm, which corresponds to the $\{1\bar{1}1\}$ plane of Ge NC with diamond structure. Figure 6(f) shows the size distribution of the Ge NCs embedded in an Al_2O_3 matrix (figure 6(e)). The size distribution of the NCs for the Al_2O_3 -embedded sample can be approximated by Gaussian nature with an average diameter of 12.9 nm. The change in Gibbs free energy of formation of GeO ($-111.8 \text{ kcal mol}^{-1}$) is much smaller than that of high- k oxides, such as HfO_2 ($-260.1 \text{ kcal mol}^{-1}$) and Al_2O_3 ($-378.2 \text{ kcal mol}^{-1}$), which results in the oxidation of Hf or Al and agglomeration of Ge atoms into NCs during thermal annealing at high temperatures.

5.2.2. Chemical and interfacial properties. X-ray photoelectron spectroscopy (XPS) has been widely used to

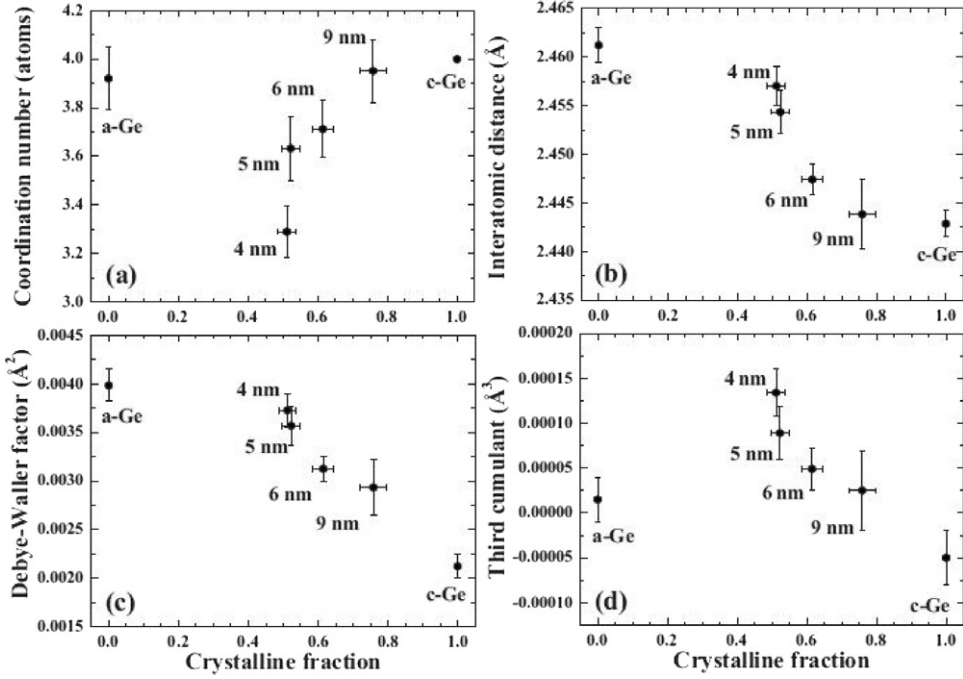


Figure 8. The first shell (a) coordination numbers, (b) interatomic distances, (c) Debye–Waller factors, and (d) third cumulants, plotted as a function of the size-dependent crystalline fraction in Ge NCs using XANES and EXAFS measurements. (Reprinted with permission from The American Physical Society: [122], copyright 2008).

investigate the growth mechanism of Ge NCs in oxide matrices through the study of binding energy of core-level electrons. Figure 7(a) shows the typical high-resolution XPS spectra of Ge 3d core-level electrons for HfO₂-embedded Ge NCs, in as-deposited and annealed samples, at a depth of ~ 27 nm from the surface of the film. All the spectra are fitted by three Gaussian peaks for Ge oxidation states [58, 124, 125] to analyse the chemical bonding and composition. The first one is assigned to the metallic Ge (Ge⁰) around 29.1 eV, while the remaining peaks at higher binding energies are related to oxide components inhabited in the interface separating the NCs from the high- k oxide matrix or dissolved in the matrix [125–127]. From the table in the inset of figure 7(a), it is found that Ge concentration is much more in the annealed samples compared with the as-deposited one. A reduction in the concentration of GeO₂ and GeO is observed for annealed samples. The reduction in suboxide concentration leads to an increase in the Ge concentration in the film. Thus, the formation of Ge NC most likely originates from the dissociation of suboxides and agglomeration of Ge during N₂ annealing. Figure 7(b) shows the binding energy spectra for Hf 4f electrons for as-deposited and annealed samples. The deconvoluted spectra exhibit two peaks at 18.4 eV and 16.8 eV attributed to the binding energy of Hf 4f_{5/2} and Hf 4f_{7/2}, respectively. The binding energy separation of 1.6 eV corresponds to the formation of Hf–O bonds [128]. The spectra yield no indication of Hf in a metallic or silicided phase (binding energy 14.2 eV). There is no change in the peak position and intensity for the as-deposited and annealed samples, which confirms the existence of only Hf–O bonds. The study shows that post-deposition annealing plays a crucial role in the formation of Ge NCs in oxide matrices.

5.2.3. Microstructural properties of Ge NCs. Synchrotron-based structural property investigations using x-ray-absorption near-edge structure (XANES) and extended x-ray-absorption fine structure (EXAFS) have been reported [122] to be useful in investigating the amorphous and crystalline fractions in Ge NCs as a function of their size. XANES/EXAFS measurements at the Ge *K* edge (11.103 keV) provide the structural parameters for the first three nearest-neighbour (NN) shells surrounding Ge. Figures 8(a), (b), (c) and (d), respectively, present the first shell coordination numbers, interatomic distances, Debye–Waller factors and third cumulants, as a function of the crystalline fraction in Ge with different sizes [122]. The finite size effect is clearly evident in figure 8(a) showing the decrease in coordination number with a reduction in NC size, since the increase in surface-to-volume ratio yields a relative increase in under-coordinated surface atoms. On the other hand, as shown in figure 8(b), the interatomic distance decreases with the increase in the size of the NCs and approaches the value for bulk Ge (c-Ge) for 9.0 nm diameter NCs. This is in disagreement with the results reported for metallic NCs [129], indicating that the increase in amorphous fraction of semiconductor NCs with decreasing size may be the origin of the observed discrepancy. The plot of Debye–Waller factor in figure 8(c) shows an increase in structural disorder with decreasing NC size indicating that the behaviour approaches that of amorphized Ge NCs, as the crystalline fraction becomes negligible. The increased asymmetry in the interatomic distance distribution of the first NN shell with the increase in the surface-to-volume ratio for Ge NCs is apparent from the distribution of non-zero third cumulant value shown in figure 8(d). The above observation indicates that very small

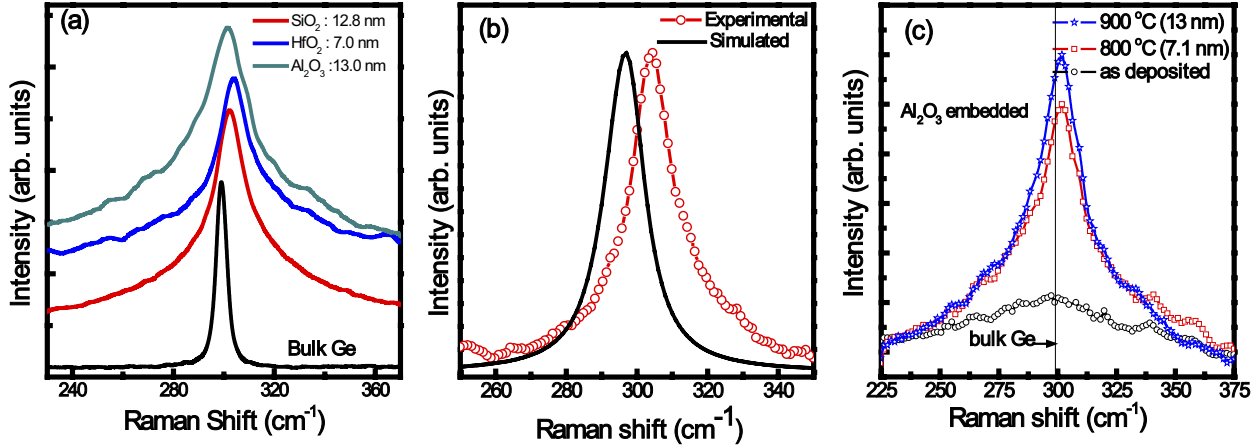


Figure 9. Raman spectra for (a) Ge bulk and Ge NCs of given NC sizes embedded in different dielectric matrices, (b) Ge NCs embedded in HfO₂ for 900 °C annealed (o) and solid line is the phonon confinement simulation for the case of fully relaxed NCs [58], (c) Ge NCs embedded in an Al₂O₃ matrix in the as-grown and post-growth annealed samples (57).

sized Ge NCs (below 2.0 nm) embedded in a silicon oxide matrix may be amorphous in nature, as predicted [130] for embedded Si NCs with molecular-dynamics simulation.

5.3. Vibrational properties and stress in embedded NCs

Raman spectroscopy is useful in studying the vibrational properties of Ge NCs as the asymmetric broadening of the Raman band is characteristic for low-dimensional structures. The frequency of the phonon band depends on the mass and position of the atoms, inter atomic forces and the bond length. Therefore, any effects altering these features will produce a change in the frequency of the Raman band. For semiconductor NCs, the spatial confinement of phonons leads to the partial relaxation of the wave-vector selection rules, causing modifications in the bulk Raman characteristics. Therefore, a shift of the optical phonon peak position of germanium NCs with respect to bulk can be caused by several effects: isotopic composition [131], phonon confinement [132–134] and stress [58, 135–137]. For sputter-deposited samples, there is no change in the isotopic composition of germanium. This is the reason why the band position is sensitive to the presence of stress and phonon confinement in NCs. By evaluating the Raman peaks of the embedded and exposed NCs, it is possible to obtain quantitative estimation of the stress of the embedded NCs [58, 135]. Figure 9(a) shows the Raman spectra of bulk Ge and Ge NCs embedded in different dielectric matrices after post-growth thermal annealing at 900 °C in N₂ atmosphere. Raman spectra of NCs are characterized by the size-dependent phonon confinement effects which, for the case of Si and Ge, are manifested by asymmetric line broadening and redshift of the peak due to breakdown of the $k = 0$ selection rule for Stokes scattering. The scattering peak at around 300 cm⁻¹ is attributed to the crystalline Ge–Ge phonon vibration mode. The spectrum for embedded Ge NC samples exhibits the expected asymmetric broadening in the lower wave number due to phonon confinement. However, the blueshift of the peak position with respect to that of the bulk reference spectrum is in disagreement with the prediction of phonon confinement

theory. A similar blueshift of Raman spectra of silica-embedded [135, 136] and sapphire-embedded [137] Ge NCs has been reported, and is attributed to the matrix-induced compressive stress on embedded NCs. The stress could arise due to the volumetric expansion of Ge during solidification [136], fast growth rate experienced by NCs as a result of enhanced diffusivity [137] and from the interface energy. The hydrostatic pressure P in the NCs can be estimated as [138]

$$P = \frac{(\omega_{\text{stressed}} - \omega_{\text{relaxed}})}{3\gamma\omega_0(S_{11} + 2S_{12})}, \quad (8)$$

where ω_{stressed} , ω_{relaxed} and ω_0 are the Raman shifts of stressed NCs embedded in SiO₂, relaxed NCs and pure bulk Ge, respectively, $\gamma = 0.89 \text{ cm}^{-2}$ is the mode-Grüneisen parameter, and S_{11} and S_{12} are components of the elastic compliance tensor with $S_{11} + 2S_{12} = 0.44 \times 10^{-12} \text{ dyne}^{-1} \text{ cm}^2$ [138]. The relaxed line position is calculated using the phonon confinement model developed by Richter *et al* [132]. According to this model, the first-order Raman spectrum of a NC can be described as a weighted contribution of phonon Lorentzians:

$$I(\omega) \propto \int \frac{|C(0, q)|^2}{[\omega - \omega(q)]^2 + (\frac{\Gamma_0}{2})^2} dq, \quad (9)$$

where q is the wave vector, $\omega(q)$ is the phonon dispersion curve, Γ_0 is the natural line width of the corresponding bulk material and $C(q)$ is the Fourier coefficient of the weighting function described as

$$|C(0, q)|^2 = \exp\left(\frac{q^2 L^2}{16\pi^2}\right), \quad (10)$$

where L is the NC diameter. An expression for the average phonon dispersion of Ge within the Brillouin zone, $\omega(q)$, is calculated using the Brout sum method and neutron scattering data of Nilsson and Nelin, as [136]

$$\omega(q) = \left(\omega_0^2 - \frac{43565q_r^2}{|q_r| + 0.5766}\right)^{1/2}, \quad (11)$$

Table 1. Raman peaks for relaxed (phonon confinement model) and embedded (experimental) Ge NCs in different matrices along with estimated hydrostatic stress.

| Matrix/anneal temp. | NC distribution | | Ge–Ge phonon peak position | | Stress GPa |
|---|-----------------|-----------|--|---|------------|
| | Diameter (nm) | FWHM (nm) | Experimental embedded (cm^{-1}) | phonon confinement relaxed (cm^{-1}) | |
| SiO ₂ (900 °C) | 12.3 | 2.1 | 302.7 | 298.2 | 1.6 |
| HfO ₂ (900 °C) | 7.0 | 2.6 | 304.9 | 296.3 | 2.3 |
| Al ₂ O ₃ (900 °C) | 13.0 | 2.0 | 301.2 | 298.4 | 0.8 |
| Al ₂ O ₃ (800 °C) | 7.1 | 0.5 | 301.5 | 297.4 | 1.2 |

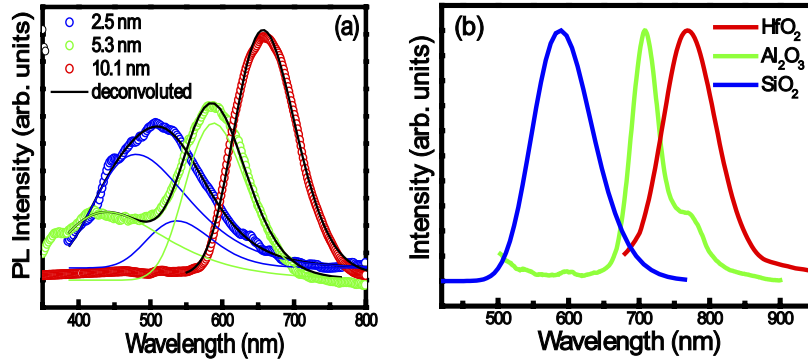


Figure 10. Room-temperature photoluminescence from Ge NCs (a) embedded in an SiO₂ matrix with average sizes of 2.5 nm (800 °C annealed), 5.3 nm (900 °C annealed) and 10.1 nm (1000 °C annealed) [144], and (b) NCs with average sizes of 5.3 nm, 7.1 nm and 7.8 nm embedded in SiO₂, Al₂O₃ and HfO₂ matrices, respectively [144].

where $q_r = (a/2\pi)q$ is the reduced wave vector, a is the lattice parameter of bulk Ge, and ω_0 is the bulk zone centre optical phonon frequency for isotopically enriched bulk ⁷⁴Ge. Figure 9(b) shows the experimental Raman spectrum of the HfO₂-embedded Ge NC sample (900 °C annealed) along with a simulated spectrum (solid line) calculated according to equation (9) with Fourier coefficients and phonon dispersion curve given by equations (10) and (11), respectively. The average diameter of NCs is taken as 7.0 nm. Figure 9(c) shows the Raman spectra for Al₂O₃-embedded Ge NC samples under as-deposited and annealed conditions. The calculated Raman peaks for relaxed Ge using the phonon confinement model in comparison with the experimental values for embedded Ge NCs for different samples are summarized in table 1. The hydrostatic pressure P calculated using the above values from equation (8) for different samples is also presented in table 1. From the table it is observed that with the increase in annealing temperature from 800 to 900 °C, the stress decreases from 1.2 to 0.8 GPa for an Al₂O₃-embedded NC. A similar type of stress relaxation has also been observed in SiO₂ [135, 139] and HfO₂ [58] embedded NCs. The stress relief process is governed by the diffusive flux of matrix atoms away from the local NC growth region [135]. The stress relaxation mechanism has been reported in detail for SiO₂-embedded Ge NCs [135] in the literature.

5.4. Optical properties of Ge NCs

5.4.1. Photoluminescence characteristics. In contrast to bulk indirect semiconductors, no-phonon transitions may be possible in NCs due to the confinement of electron and

hole wave functions in real space that leads to their spread in momentum space. For Ge, most reports of visible and near-infrared photoluminescence from low-dimensional structures involved Ge NCs embedded in an SiO₂ matrix [32, 33, 65, 73–75, 110, 140, 141]. In comparison with Si, Ge has a larger effective Bohr radius for Wannier excitons (~24.3 nm), making it attractive to study the optical properties with strong confinement for NC size of around 10–15 nm. The light emission mechanism from Ge NCs has been discussed extensively, which is attributed either to radiative recombination via quantum confined states [31, 73, 74, 110, 137, 140] or to defects at the NCs/matrix interface and in the matrix itself [32, 33, 125]. Figure 10(a) presents the room-temperature photoluminescence spectra of SiO₂-embedded Ge NCs deposited by rf sputtering as a function of their size. The as-deposited SiO₂/SiGe/SiO₂ trilayer thin film was annealed at 800 °C, 900 °C and 1000 °C for 30 min in N₂ to form Ge NCs of average diameter 2.5 nm, 5.3 nm and 10.1 nm, respectively. For a closer insight into the PL results, the spectra are deconvoluted using Gaussian function, as shown by solid lines in figure 10(b). For the 800 °C annealed sample the PL spectrum consists of two peaks centred at 536.8 and 480.6 nm. Similarly, for the 900 °C sample the PL spectrum can be represented by two peaks centred at 589.3 and 442.8 nm. On the other hand, the 1000 °C annealed sample shows a single and sharp luminescence at 658.5 nm. The appearance of PL peaks at 536.8, 589.3 and 658.5 nm can be explained in accordance with the quantum size effect, having average Ge NC diameters of 2.5 nm, 5.3 nm and 10.1 nm, respectively. Hence, the above PL peaks originate due to the radiative recombination of excitons in

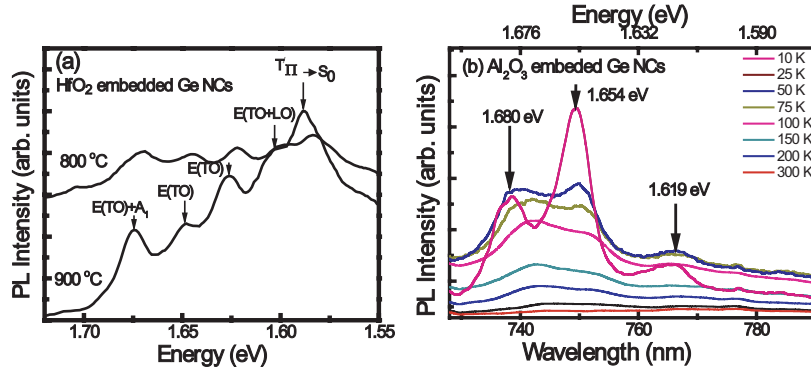


Figure 11. Phonon structures in photoluminescence spectra at 25 K around 1.58 eV from surface oxidized Ge NCs embedded in an HfO₂ matrix annealed at 800 °C and 900 °C [125]. (b) Temperature-dependent PL spectra from Al₂O₃-embedded Ge NCs showing the fine structures related to phonons.

quantum confined Ge NCs. However, the appearance of emission peaks at 480.6 nm and 442.8 nm for NC size of 2.5 nm and 5.3 nm, respectively, contradicts the simple QC model. Several researchers [32, 33, 142] have reported size-independent photoluminescence in the wavelength range 380–490 nm from germanium NCs, the origin of which is attributed to oxygen vacancies (V_O[−]), oxygen–germanium vacancy pairs (V_{Ge}, V_O)⁺ and related defect centres. It is thus very plausible that the defects in the SiO₂ matrix region or the interface between the SiO₂ and Ge NCs are responsible for the observed size-independent visible PL peaks at 480.6 nm and 442.8 nm for 800 °C and 900 °C annealed samples, respectively. The PL intensity of the defect-related peak is significantly reduced, and that of excitonic recombination is enhanced with the increase in annealing temperature to 1000 °C, due to reduced interface defects and improved crystallinity of Ge NCs. In addition to the emission in the blue and green regions, violet photoluminescence bands have also been observed from Ge NCs in SiO₂ matrix prepared by an implantation route [143].

We have also reported the experimental results on the effect of host matrix on the emission characteristics of embedded Ge NCs [144]. The dissimilar confinement potential acting on carriers confined in NCs, due to different conduction and valence band offsets of SiO₂, HfO₂ and Al₂O₃ matrices, respectively, may affect the emission peak position [144, 145]. Figure 10(b) shows the effect of host matrix on room-temperature photoluminescence spectra of 900 °C annealed Ge NCs of sizes 5.3 nm, 7.1 nm and 7.8 nm embedded in SiO₂, Al₂O₃ and HfO₂, respectively. Intense broad emission peaks are observed around 589.3 nm (2.11 eV), 709.1 nm (1.75 eV) and 770.3 nm (1.61 eV) for SiO₂--, Al₂O₃- and HfO₂-embedded Ge NCs samples, respectively. The size-dependent emission peak shift is also clearly observed with Ge NCs in different host matrices, following the QC model. A simple confinement model [141] is applied by considering electrons and holes confined independently in quantum dots of radius, *R*:

$$E_{nl} = E_g + \frac{\hbar^2}{2\mu_{e-h}} (\alpha_{nl}/R)^2 - 1.786e^2/kR, \quad (12)$$

where the second term represents the kinetic energy of electrons and holes while the last term denotes the Coulomb

interaction term. μ_{e-h} is the reduced mass of excitons, *k* is the static dielectric constant (for Ge *k* = 16.3), α_{nl} is the eigenvalue of the zeroth-order spherical Bessel function ($\alpha_{10} = \pi$) and the band gap energy of Ge $E_g = 0.66$ eV. The calculated sizes of Ge NCs according to the QC model (using equation (12)) are 5.9 nm, 6.6 nm and 7.1 nm for PL peak energies 2.11 eV, 1.75 eV and 1.61 eV, respectively. It may be noted that the above simple confinement model does not consider the matrix effect in terms of either the confinement potential or the matrix-induced stress. Therefore, the observed difference in the size of Ge NCs between the theoretical (QC model) and experimental (TEM) values may be attributed to the combined effect of confinement potential and matrix-induced stress on the NCs.

The surface and interface atoms play dominant roles as the size of the NC decreases, which determine the magnetic, optical, electrical and electro-optical properties due to the enhanced surface-to-volume ratio [146–147]. The coupling of electronic and vibrational excitations dramatically increases with the localization of excitons and QC in smaller dimensions [148, 149]. The optical and electrical properties of semiconductors are significantly influenced by this coupling, as it determines the transport behaviour and energy relaxation rate of excited carriers. There exist only a few reports showing the fine structures [125, 147] in the PL spectrum of Ge due to strong coupling of excitons. Figure 11(a) shows the reported low-temperature PL spectra of HfO₂-embedded Ge NCs having sizes 5.2 nm and 7.5 nm for 800 °C and 900 °C annealed samples, respectively. In addition to the T_{II} → S₀ (1.588 eV) level transition in GeO molecules, additional fine structures are observed at 1.603, 1.627, 1.648 and 1.675 eV for both the annealed samples. Based on the observed temperature dependence and measured energy separation, the peaks are related to the E(TO+LO), E(TO), E(TO) and E(TO)+A₁ phonon lines of GeO₂ [150] having energies 15 meV, 39 meV, 60 meV and 87 meV, respectively. Second-order phonon structures are also observed on the higher energy side of the UV-PL peak (3.18 eV). The 3.18 eV UV peak is related to optical transitions from the triplet state T_π or T_Σ to the ground state (S₀) of GeO colour centres [149]. From the XPS results, it is observed that the Ge NCs are surface oxidized ones. The fine structures related to GeO₂ confirm

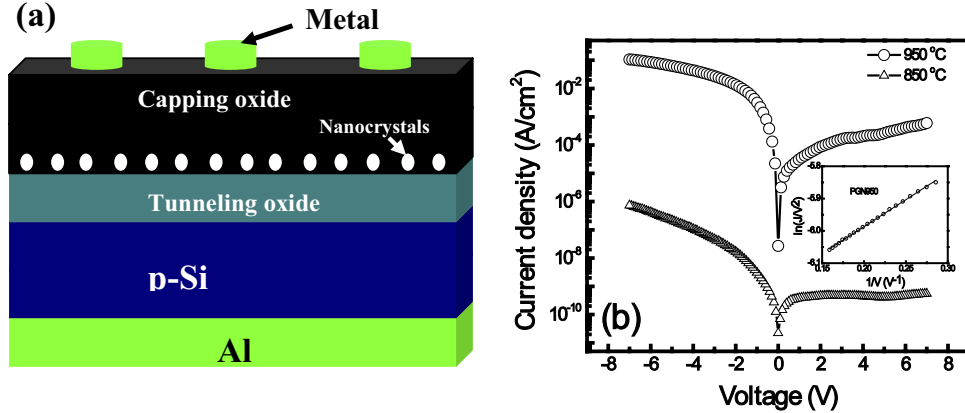


Figure 12. (a) Schematic diagram of a Ge NC based MIS LED structure, (b) current density–voltage characteristics of the Ge NC embedded MIS structures annealed at 850 °C and 950 °C.

the coupling of localized exciton on the surface of the NCs with phonon vibrations. Figure 11(b) shows the temperature-dependent PL spectra of 6.2 nm Ge NCs embedded in an Al₂O₃ matrix. The splitting of PL peak is observed at very low temperatures. At 10 K, the PL spectrum shows three distinct peaks at 1.680, 1.654 and 1.619 eV. Now the energy difference between the first and second peaks is 28 meV, and that between the second and third peaks is 35 meV. It may be noted that the Ge–Ge TO phonon energy is 36 meV, and the GeO₂ A₁ phonon has an energy of 26.3 meV [150]. Hence the PL peak at 1.654 eV belongs to the NP peak of Ge NCs and the 1.619 eV peak is related to the Ge–Ge TO phonon assisted transition, whereas the 1.680 eV peak is related to the GeO₂ A₁ phonon. For this Al₂O₃ sample both Ge and GeO₂ related phonon structures are observed. The observed phonon structures in low-temperature PL spectra from surface oxidized Ge NCs prove the existence of strong interaction between electronic excitons and the localized vibrations of GeO₂ and Ge.

5.4.2. EL characteristics of Ge NCs. Optically active engineered germanium nanostructures with high EL efficiency are required for their applications in LEDs. The effect of Ge NC size and distribution on the EL spectra has been studied [106]. The reported size-independent EL peak at 590 nm from Ge NC MIS structures [151] could have originated due to the defect-mediated emission. Kanjilal *et al* [152] observed the defect-engineered blue–violet EL from Ge NC rich SiO₂ layer by Er doping. The EL properties of Ge NC based MIS device structures are discussed here. The light-emitting structure was formed by fabricating MIS capacitors with a dielectric stack consisting of Ge NCs sandwiched between tunnelling and capping oxides. Figure 12(a) shows the schematic diagram for the Ge quantum dot MIS LED structure. A critical challenge for MIS NC LED is to achieve efficient carrier injection [94, 153] through the tunnel oxide. Figure 12(b) shows the current density versus voltage (*J*–*V*) characteristics of the embedded Ge-NC samples. The positive gate voltage represents the reverse bias for which the depletion and inversion layers are formed in the sample. On the one hand, a forward bias is created for the negative gate voltage driving the device into an accumulation mode. The device conductivity

increases to a large extent when the Ge NC content increases in the active layer. Since the 950 °C annealed sample has larger sized Ge-NCs than the 850 °C one, its conductivity is larger both in forward and reverse bias. The conduction mechanism among the gate-dielectric stack with Ge NCs is explained by the F–N tunnelling [154], in which the current density (*J*) can be expressed as

$$J = E^2 \exp \left[\frac{8\pi \sqrt{2m^*} (q\phi_B)^{3/2}}{3qhE} \right], \quad (13)$$

where *E* is the applied electric field, *m** is the electron effective mass, *h* is the Planck constant, Φ_B the energy barrier at the injecting interface. The inset in figure 12(b) shows the plot of ln(*J*/*V*²) versus 1/*V* for the sample annealed at 950 °C. A linear region of the plot at high field indicates that the conduction mechanism is governed by F–N tunnelling for Ge dots embedded in the oxide stack. The shape of the *J*–*V* characteristics is similar to those reported for Si-NC-based MIS LEDs [155]. There are two dominant current injection mechanisms in Ge-NCs: (i) unipolar tunnelling of hot electrons followed by impact ionization of the Ge-NCs [156], and (ii) bipolar tunnelling of electrons and holes in the same Ge-NC [94].

Figures 13(a) and (b) show the room-temperature EL spectra at different injected currents for Ge NCs embedded in an Al₂O₃ gate MIS structure annealed at 850 °C and 950 °C, respectively. The average Ge NC size is found to be 3.0 nm and 6.1 nm, respectively. For the 850 °C annealed device (size ~3.0 nm) in figure 13(a), the EL spectrum can be fitted by three Gaussian peaks centred at 586 nm, 691 nm and 824 nm and having FWHM of 81 nm, 102 nm and 78 nm, respectively. Similarly, the EL spectra of the 950 °C annealed sample (size ~6.1 nm) in figure 13(b) can be fitted by three Gaussian peaks centred at 629 nm, 736 nm and 878 nm with FWHM of 122 nm, 107 nm and 84 nm, respectively. The peaks are blue shifted in the device with smaller Ge-NC size, as expected by the quantum size effect. The presence of more than one EL peak can be either due to the size distribution of Ge NCs or to different recombination mechanisms. In particular, if this last hypothesis is valid, one can tentatively assign the most intense

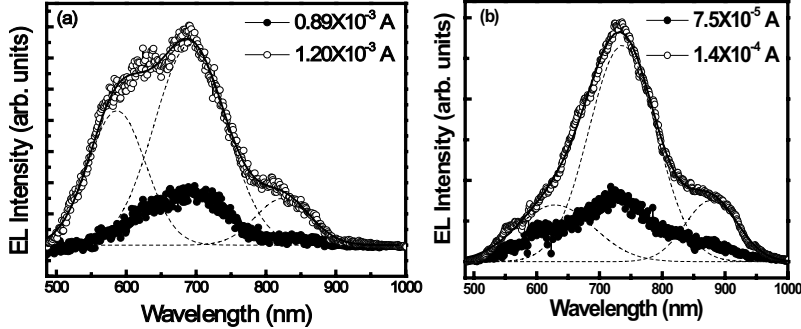


Figure 13. Room-temperature EL spectra from Al_2O_3 -embedded Ge NC MIS structure annealed at (a) 850°C (NC diameter 3.0 nm) and (b) 950°C (NC diameter 6.1 nm) for different injected currents.

EL peak at 691 nm (736 nm) to electron–hole recombination in Ge NCs in Al_2O_3 , the weaker EL peak at 586 nm (629 nm) to defect-related recombination at the Ge NC/ Al_2O_3 interfaces [104, 105], and the very weak peak at 824 nm (878 nm) to oxygen-related defects in GeO_2 for 850°C (950°C) annealed samples. On plotting the integrated EL intensity (I_{EL}) as a function of the drive current density (J), the onset voltage for EL is found to be 3.7 V and 14.4 V for the 950°C and 850°C annealed samples, respectively. The lower onset voltage for the 950°C annealed device is due to the higher tunnelling current as compared with that for the 850°C annealed one because of the formation of larger sized NCs in the former. This is also in agreement with the reported results for Si NC based MIS LEDs [96]. A power law characteristic is observed for the integrated EL intensity (I_{EL}) as a function of injected current density (J), as

$$I_{\text{EL}} \sim J^\alpha. \quad (14)$$

The power law exponent α is found to be 1.1 ± 0.1 and 1.4 ± 0.1 for the 950°C and 850°C annealed samples, respectively. The larger α value for the 850°C annealed sample (size ~ 3.0 nm) points to a relatively larger defect density [157] due to the presence of higher fraction of a-Ge in small-sized NCs, which is corroborated by the microstructural properties discussed in section 5.2.3.

6. Rare-earth-doped Si and Ge NCs

Among different strategies to realize light emission from silicon-based materials, the rare-earth doping [158–162] methodology has dominated for the development of photonic devices. Doping with erbium and ytterbium has been studied extensively due to the strong emission lines around 1540 nm and 980 nm from intra-f shell transitions in Er^{3+} and Yb^{3+} , respectively [159–163]. The possibility of variable wavelength emission from silicon structures can extend the technological interests to many other rare-earth elements such as Tb [164], Eu [165] and Ce [168], with broad band emission in the UV to visible range. As Er-induced emission occurs at the telecommunication wavelength ($1.54\text{ }\mu\text{m}$), the dopant is a natural choice for devices requiring optical gain for Si-photonics.

The origin of Er^{3+} luminescence at $1.54\text{ }\mu\text{m}$ is due to intra-4f transition from the first excited to the ground state

(${}^4\text{I}_{13/2} \rightarrow {}^4\text{I}_{15/2}$). Unfortunately, this transition is parity forbidden for the free ion or in a host with inversion symmetry. The initial research was focused on Er doping in bulk silicon [166, 167] and silicon oxide [168]. But luminescence from Er-doped bulk silicon is limited due to strong thermal quenching leading to very short lifetime [167] of the optical transition. The emission from rare-earth-doped silicon oxides also has problem related to inefficient excitation of intra-4f transitions from rare-earth ions and low solubility of optically active rare-earth ions in silicon-based hosts. A plausible way to solve this problem is to incorporate Er within Si or Ge NCs [37–39, 168, 169] embedded in an oxide matrix. The NC sensitizers allow efficient room-temperature Er^{3+} luminescence due to enhanced charge transfer to rare-earth ions. The oxide matrix with a much higher band gap also leads to enhanced optical activation of Er^{3+} ions, compared with bulk Si with low absorption loss. Therefore, Er-doped Si/Ge NCs in an oxide matrix are attractive for the fabrication Si-based LEDs at communication wavelength and operating at room temperature [170–175]. The transition of Er^{3+} from the ${}^4\text{I}_{15/2}$ ground state to various excited states gives rise to different absorption edges. Following the first report [176] of the strong enhancement of $1.54\text{ }\mu\text{m}$ emission using crystalline Si-NCs in silica, Er-doped Si nanostructures have been extensively studied [37, 162, 168, 169, 177, 178]. The introduction of Si NCs enables indirect excitation of Er^{3+} ions and this process is non-resonant with an effective excitation cross section of $\sigma \sim 10^{-17}\text{--}10^{-16}\text{ cm}^{-2}$ [168]. Förster dipole–dipole mechanism [179] apparently dominates the energy transfer from Si NCs to Er^{3+} levels. The lifetime varies from the microsecond range for NC-mediated Er^{3+} excitation to a much faster (100 ns range) one.

Figure 14 shows the schematic description for the reported interaction model between Si NC and Er^{3+} ion, with related excitation and de-excitation mechanisms of carriers [180, 181]. As soon as a Si-NC with absorption cross-section σ_{Si} absorbs the incident pump photons with a flux φ , carriers are generated, and the excited electrons are eventually trapped at interfacial states (process (i) in figure 14). The recombination of the electron in the interfacial state with a hole in the valence band gives rise to emission of photon, which is then transferred to the Er ion exciting it to the ${}^4\text{I}_{9/2}$ level (dotted circle in process (ii)). In addition to Er^{3+} excitation, the excitation/de-excitation of Si NCs as marked (v) in figure 14 and the interaction between

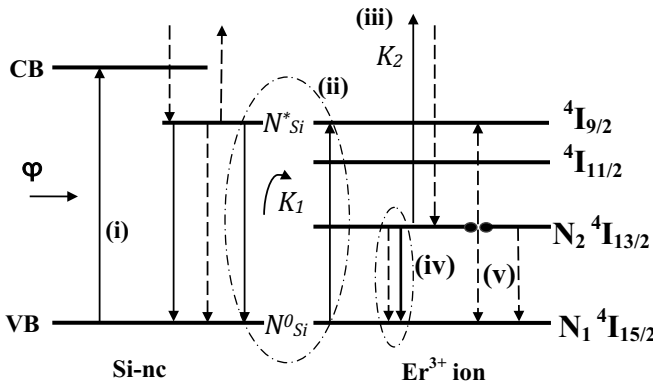


Figure 14. A schematic description for the reported interaction model between Si NC and Er^{3+} ions, with related excitation and de-excitation mechanisms of carriers.

Si-NC and Er^{3+} ions also take place [39]. The energy scheme of Si NC can be regarded as a quasi-two-level system. NCs promote the exciton generation at a rate given as $\sigma_{\text{Si}}\varphi$. When Si-NCs are coupled to Er^{3+} ions, the energy due to excitonic recombination is transferred to the Er^{3+} ions, allowing the carriers in Er to higher excited states from the ground state (N_1). This is shown with the arrow in process (ii). The loss mechanism involves the excited-state absorption (ESA), where an excited Er is pumped to a higher level by the energy transfer from the recombination of an excited Si NC, as shown with process (iii) in figure 14. The rate equation for Si NC coupled subsystem is given by [180, 182],

$$\frac{dN_{\text{Si}}^*}{dt} = \sigma_{\text{Si}}\varphi N_{\text{Si}}^0 - \frac{N_{\text{Si}}^*}{\tau_{\text{Si}}} - K_1 N_1 N_{\text{Si}}^* - K_2 N_2 N_{\text{Si}}^*, \quad (15)$$

where N_{Si}^* is the density of the excited Si NC, N_{Si}^0 the Si NC in the ground state, K_1 is the coupling constant between Si NC and Er in the ground state and K_2 is the coefficient for ESA. Resonantly excited Er^{3+} ions by direct absorption also non-radiatively relax to the $4I_{13/2}$ level and then can decay radiatively to the $4I_{15/2}$ level (dotted circle marked (iv) in figure 14). In the low pump flux regime, it is apparent that most Er^{3+} ions are in the ground state so that de-excitation processes of excited Er^{3+} are small. Then the rate equation for Er^{3+} ions in the first excited (N_2) state in the coupled system is given by [182]

$$\frac{dN_2}{dt} = \sigma_{\text{eff}}\varphi N_1 - \frac{N_2}{\tau_{\text{PL}}}, \quad (16)$$

where σ_{eff} is the effective cross section, a value depending on σ_{Si} , K_1 , K_2 and φ . The expression for σ_{eff} can be found in [182]. Under steady-state conditions, the population of excited Er^{3+} in the low pump regime is finally given by [182]

$$N_2 = \frac{N_0\varphi}{\varphi + 1/\sigma_{\text{eff}}\tau_{\text{PL}}}, \quad (17)$$

which is the typical sigmoidal curve that defines the population of a simplified two-level system. Figure 15(a) shows reported [181] results on room-temperature PL spectra of three different samples consisting of (i) Er-doped Si NCs (continuous line),

(ii) Er-doped SiO_2 matrix (dashed line) and (iii) Si NCs without Er doping (short dashed line), which shows an increase in PL intensity by a factor of 10^3 [181] for the NC sample. A difference in excitation wavelength dependence for the sample containing Si NCs and the control sample has been reported [160]. The control sample without Si NCs exhibits a distinct peak at 488 nm, corresponding to the $4I_{15/2}-4F_{7/2}$ transition of Er^{3+} . On the other hand, no distinct feature is observed in Er-doped NCs, indicating that the excitation is mostly by the absorption by Si NCs and the subsequent energy transfer to Er^{3+} . Figure 15(b) shows the reported experimental and simulation data [182] showing the number of rare-earth atoms in the excited state for the Er-doped Si-rich silica layer annealed at 900 °C for 60 min. The number of Si-NCs coupled to a single Er ion is still a debatable issue (between one and ten) [183], indicating the defect-mediated energy transfer as the dominant mechanism [16, 178]. The first Er-doped LED was reported [184] to operate at 77 K giving emission at $1.54\ \mu\text{m}$. Room-temperature Er-doped Si NC LEDs with an external quantum efficiency (EQE) larger than 0.1% at $1.54\ \mu\text{m}$ have been demonstrated [185–187]. The host matrix also influences the performance of Er-doped Si [38] nanocluster LEDs. Bipolar pulsed excitation is a solution to overcome non-radiative Auger de-excitation of Er in Si NC : Er LEDs [188]. A modal gain of 2 dB cm^{-1} under pulsed excitation in a slot waveguide confined Si NC : Er [189] has also been reported. Figure 16 shows the reported [190] EL spectral response for Si NC LEDs with and without Er doping after bipolar pulsed excitation. The observed saturation of the $1.54\ \mu\text{m}$ emission in figure 16 is due to the limited number of optically active Er ions and to the onset of non-radiative recombination processes [188]. The EQE value of Er-doped Si-NC LED emitting at $1.54\ \mu\text{m}$ shown in figure 16 is among the best values reported so far for Er-doped silicon LEDs (see for example [191]).

Matrix containing Ge NCs is an attractive alternate host for reducing the interband self-absorption of $1.5\ \mu\text{m}$ emission in Er-doped NCs. The size-dependent optical absorption edge of Ge nanoparticles can be exploited [192, 193] in reducing the self-absorption of the Ge : Er luminescence at $1.5\ \mu\text{m}$. A stronger QC and resultant increase in exciton binding energy in Ge is also useful in achieving enhanced radiative recombination in NCs. In addition, Ge exciton energy is close to the $1.54\ \mu\text{m}$ transition of Er ions, which may be useful in improving the pumping efficiency. The energy back transfer [194, 195] from excited Er^{3+} to Ge NCs is predicted to be strongly reduced with the reduction in the size of Ge NCs. Although a large number of research studies have been carried out on Er-doped Si nanostructures, there exist only a few reports on the luminescence characteristics of Er³⁺-doped Ge NCs [40, 41, 195–199]. Room-temperature photoluminescence spectra of Er-doped Ge NCs in a silicon oxide matrix in comparison with that of Er-doped control sample are presented in figure 17(a). A strong and broad PL peak around $1.54\ \mu\text{m}$ is observed for both the samples. The intensity of $1.54\ \mu\text{m}$ luminescence due to Er^{3+} ions is strongly enhanced in the presence of Ge NCs. It is known that the emission at $1.54\ \mu\text{m}$ originates from the transition

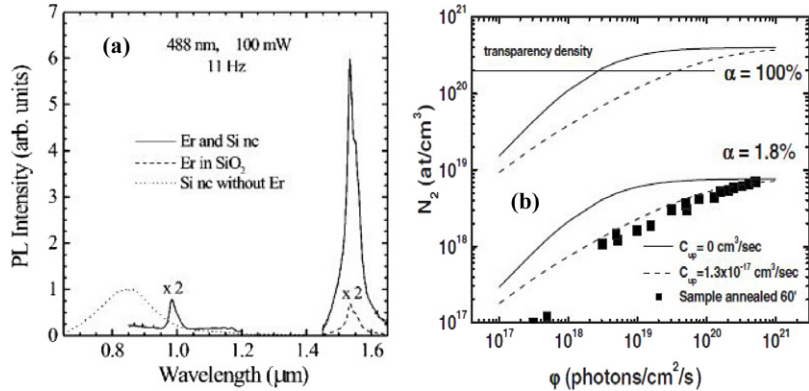


Figure 15. (a) Room-temperature photoluminescence spectra of Si NCs (short-dashed line), Er in SiO_2 (dashed line) and Er in the presence of Si NCs (continuous lines). (Reprinted with permission from The American Physical Society: [181], copyright 2003). (b) Experimental data and simulation of the number of Er atoms in the excited state for annealed Er-doped Si-rich silica layers. Solid curves account for the evolution without up-conversion and a different percentage of Er coupled to the Si nanoclusters. Dashed curves include up-conversion effects. (Reprinted with permission from The American Physical Society: [182], copyright 2007).

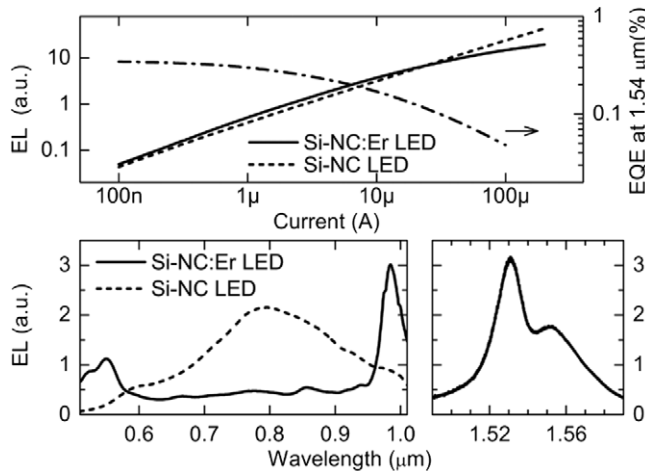


Figure 16. Integrated EL spectral intensity with wavelengths bracketing $1.54\ \mu\text{m}$ (left axis, solid line) and in the visible range (left axis, dotted line) for Si NC : Er LED and SiNC LED, respectively, as a function of the dc injected current. The dashed-dotted line shows the corresponding EQE values at $1.54\ \text{lm}$ (right axis). Bottom shows the EL spectra at an injected current of $2\ \mu\text{A}$. (Reprinted with permission from American Institute of Physics: [190], copyright 2012).

of the excited ${}^4\text{I}_{13/2}$ to the ground state ${}^4\text{I}_{15/2}$ energy levels. The strong enhancement of Er-induced PL emission can be attributed to the absorption by Ge nanoclusters, followed by an energy transfer from a trapped exciton to a nearby Er atom. PL decay characteristics at $1.54\ \mu\text{m}$ for Er-doped Ge NCs annealed at different temperatures are shown in figure 17(b). The decay time is found to be more than $10\ \text{ms}$ for Er-doped SiO_2 [180], whereas for the NC-doped sample it decreases to $6\text{--}8\ \text{ms}$. Kanjilal *et al* [200] reported enhanced blue–violet EL by inverse energy transfer to the Ge-related oxygen deficiency centres via Er^{3+} ions in MOS structures. It has been shown that Er agglomerates in the vicinity of the Ge NCs with increasing Er concentration up to 0.5% , which promotes the inverse energy transfer process [40]. For Er concentration of more than 0.5% , this effect diminishes due to the formation of the Er_2O_3 phase, which decreases the $407\ \text{nm}$ EL intensity, and the intensity of $1540\ \text{nm}$ emission increases [40].

Transparent Al_2O_3 is also a potential host matrix for rare-earth ions for optical amplifiers [201] due to its low background losses, moderate refractive index [202] and high solubility of Er [203] as compared with SiO_2 . Figure 18 shows the photoluminescence spectra of Er-doped Ge NCs in an Al_2O_3 matrix and annealed at $750\ ^\circ\text{C}$ in N_2 atmosphere for varying Er concentrations. PL measurements are made along with two control samples, one without Er and the other without Ge NC in the Al_2O_3 matrix. The control sample with only Er shows a less intense peak in the infrared spectral region at $1.54\ \mu\text{m}$. No PL emission is observed at $1.54\ \mu\text{m}$ for the Ge NC sample without Er, signifying the absence of defect-induced photoluminescence in this region. The inset of figure 18 shows the PL spectra of the Ge NCs in the Al_2O_3 matrix sample in the near infrared region [199]. A broad peak centred at $760\ \text{nm}$ is observed corresponding to an emission energy of $1.63\ \text{eV}$, which may be useful for energy transfer to Er^{3+} ions. A broad peak with intensity larger than that of the control sample without Ge is observed from the sample with Er concentration of $0.06\ \text{wt}\%$. This clearly indicates the role of Ge NCs in enhancing the PL intensity at $1.54\ \mu\text{m}$. The PL peak intensity at $1.54\ \mu\text{m}$ is found to be enhanced with increasing Er concentration up to $0.18\ \text{wt}\%$. As the concentration of Er ions is increased, more and more Er ions interact with Ge NCs, and an enhanced energy transfer from nanoparticles to Er ions takes place through Förster’s mechanism, resulting in a significant increase in the PL peak intensity. The formation of Er clusters may also result in the decrease in the PL emission [204] intensity, which can be attributed to the decreased PL intensity for higher Er concentrations ($0.25\ \text{wt}\%$). The results indicate that Er-doped Si and Ge NCs are promising candidates for Si compatible on-chip photonic devices in the communication wavelength in near future.

7. Hybrid technology: direct band gap semiconductors on silicon

Direct band gap III–V semiconductors such as GaAs and InP are widely used for efficient light-emitting sources in optoelectronic devices. Efforts have been undertaken using

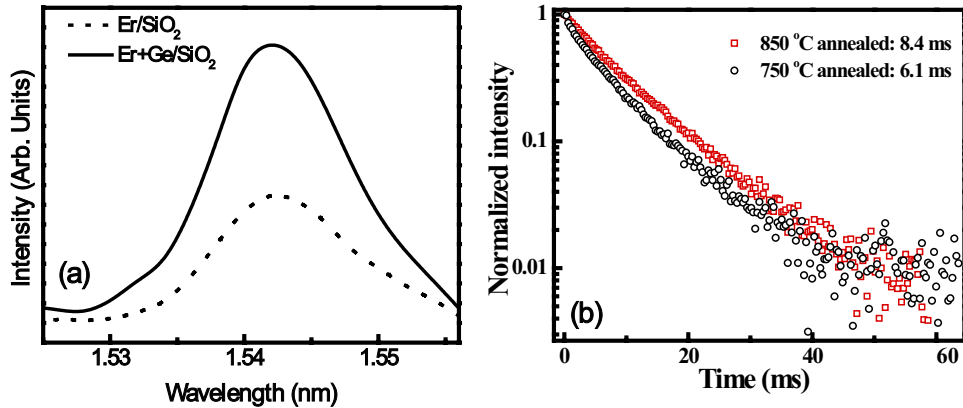


Figure 17. Room-temperature (a) photoluminescence spectra of Er-doped glass with and without Ge NCs [41], and (b) PL decay characteristics of Er-doped Ge NCs in SiO₂ prepared after annealing at 750 and 850 °C. The decay time is extracted using a single exponential fit to the time-resolved PL characteristics.

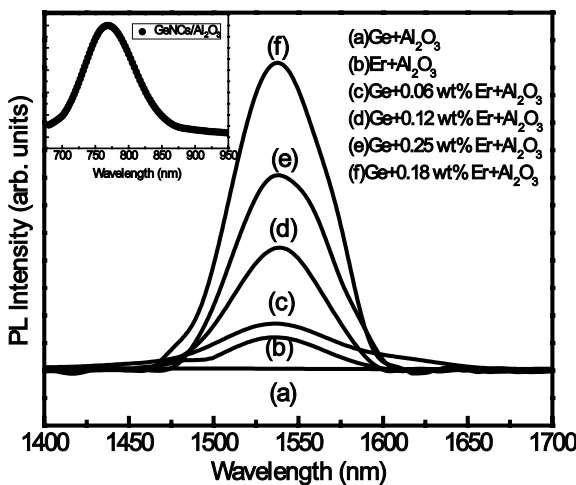


Figure 18. Photoluminescence spectra of different samples: (a) Ge NCs in an Al₂O₃ matrix, (b) Er in an Al₂O₃ matrix and (c) 0.06 wt% Er, (d) 0.12 wt% Er, (e) 0.25 wt% Er, and (f) 0.18 wt% Er doped Ge NCs embedded in an Al₂O₃ matrix [199]. The inset shows the PL emission from Ge NCs in an Al₂O₃ matrix without Er doping [199].

several challenging hybrid integration approaches such as heteroepitaxy of III–V materials directly on Si or virtual SiGe substrates [205], bonding of the III–V device wafers to Si substrates [206], wafer bonding of compound semiconductor on silicon on insulator (SOI) [207, 208] and transfer printing of epitaxial layers [209] for the successful integration of lasers on Si. A hybrid III–V electrically pumped AlGaInAs-silicon laser was first demonstrated by Fang *et al* [206] in 2006. The laser could be operated in continuous wave mode with a threshold current of 65 mA, a maximum output power of 1.8 mW with a differential quantum efficiency of 12.7% and a maximum operating temperature of 40 °C. Thereafter, an on-chip non-Fabry–Pérot cavity laser has also been reported [208]. However, the resulting III–V ELDs on Si generally exhibit extremely short lifetime and poor characteristics, due to the presence of a high density of dislocations associated with the large mismatch of lattice constants and thermal expansion coefficients as well as polar/non-polar surface incompatibility [206–209] between III–V compounds and Si. In this regard, the use of virtual SiGe substrates fabricated

Table 2. Summary of various approaches towards the development of Si-based light emitters.

| Materials/system | Wavelength (nm) | Remarks [Ref.] |
|---|-----------------|---|
| High-quality bulk Si in a solar cell | 1100 | Efficiency >1% at 200 K [211] |
| Porous silicon diode | 550–750 | EQE 1.1% [212] |
| Silicon NCs in a dielectric matrix | 750 | High optical gain [27] |
| 450–700 | EQE 0.1% [17] | |
| Nanocrystalline-Si/SiO ₂ multilayers | 700–950 | EQE 2.4% [213] |
| Efficiency 0.2% [94] | | |
| Ge NCs in a dielectric matrix | 500–850 | Room-temperature EL reported [107] |
| Er doped Si-NCs in a dielectric | | Population inversion of electrically pumped Er ions in Si nanocluster [186] |
| 0.2% tensile-strained Ge/Si p-i-n LED | 1530 | EQE 0.2% [190] |
| | 1550 | Direct band gap EL from Ge at room temperature [11] |
| III–V on Si | 1530 | Laser demonstrated [208, 209] |

using compositionally graded Si_{1-x}Ge_x layers grown on Si is an attractive alternative, because of the closer lattice matching of Ge with GaAs. Recently, CEA LETI at France has demonstrated 10 Gb s⁻¹ integrated tunable hybrid III–V/Si laser fabricated by wafer bonding [210]. Wafer-scale integration of group III–V lasers on silicon using transfer printing of epitaxial layers [209] exhibits the potential of high volume manufacturability in the near future. However, to date, the choice of useful fabrication methods, their reliability, uniformity and performance are not clear for realizing III–V-based hybrid lasers on Si substrates.

8. Silicon light emitters: future and challenges

Tremendous research progress has been made over the last few decades, raising the hope of silicon-based light emitter to a reality. Table 2 presents a summary of various approaches

undertaken towards the development of Si-based light emitters. The QC in nanostructures leads to the modification of selection rules in indirect band gap semiconductors by breaking the crystal symmetry or by phonon localization. Thus, efficient room-temperature light emission from Si and Ge NCs has been demonstrated, along with their optical gain [27, 211–213]. Efficient carrier injection in NCs confined in a dielectric matrix is yet to be achieved and the resultant wavelength does not match with the optical communication range. For display applications, the tuning of emission wavelength by changing the NC diameter is an advantage for NC-based light emitters. However, it is challenging to achieve arrays of NCs with an extremely narrow size distribution. The fabrication of mono-dispersed NCs may lead to spectrally pure colour emission from NC-based LEDs, which, however requires an innovation in growth technology. Another important issue, undoubtedly a virtue of future research, is to achieve high brightness in group-IV semiconductor NCs by overcoming the limitation of their relatively low radiative recombination rate. The luminosity and quantum efficiency can possibly be increased by coupling metal nanostructures with NCs, resulting in local-field-enhanced light emission and concomitant increase in radiative decay rate from silicon NCs.

Efficient charge injection through embedded oxides is a major bottleneck, required to be overcome for Si/Ge NC based LEDs. The control of tunnelling barrier thickness and band gap engineering of NCs using multilayer stacks may be an efficient route to increase the charge injection efficiency. Incorporating NC layers into the p–n junction injection regime may be another alternative route. Silicon or germanium NCs embedded in an insulating matrix suffer from the limited EL power efficiency, due to low conductivity and resistive heating. The controlled doping of NCs could be useful in overcoming the above problem to some extent. However, the degenerate carrier concentration in doped NCs, which may inadvertently occur in a low NC density film, will be subjected to strong non-radiative Auger recombination of injected excitons.

Erbium-doped Si and Ge NCs in a metal–oxide–semiconductor structure results in the emission in the optical communication wavelength showing high EL efficiency comparable to the commercial LEDs. An attractive approach to realizing Ge laser has been demonstrated through the modification of band structures with enhanced population of carriers in the L-valley conduction band in strained Ge on Si, resulting in increased radiative recombination efficiency. New opportunities are opening up for hybrid integration of III–V-based sources on Si substrates through heteroepitaxial growth or transfer of direct band gap epitaxial layers on Si and SOI by wafer bonding. However, significant research progress has to be made for the commercial development of Si-based lasers yielding high quantum efficiency and operating at room temperature.

9. NC-based memory devices

The FGM structure, invented by Sze and Kahng at Bell Labs in 1967, forms the primary element necessary to construct flash memories [214]. The schematic cross-section of a

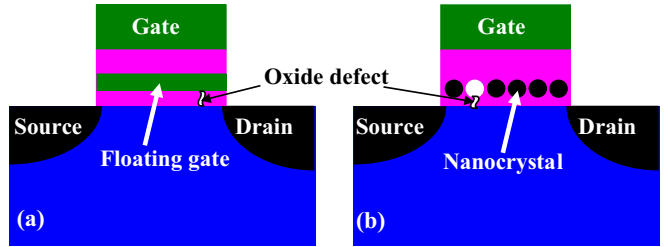


Figure 19. Schematic cross-section of the (a) conventional floating gate and (b) NC floating gate MOS memory devices.

conventional FGM device is shown in figure 19(a), with the top gate working as the control gate. The bottom gate, which is completely isolated from the outside world, is known as the floating gate and is used for charge storage. The floating gate acts as a storage node, once the charges are injected into the potential well, flanked by energy oxide barriers. The stored charges cannot discharge without an external electric field. However, the conventional flash memory suffers from charge leakage through the tunnel oxide, which is required to be very thin to achieve faster write and erase times. In conventional stacked gate devices, the charges stored in the continuous floating gate leak out even in the presence of a single defect chain, which is unavoidable in ultra-thin tunnel oxides. To alleviate the tunnel-oxide design trade-off in floating-gate devices, MOS memory cells employing semiconductor and metal NC charge-storage sites embedded within the gate dielectric have evolved. Discrete NCs as charge storage nodes were first proposed by Tiwari *et al* in 1996 [45]. Figure 19(b) shows the schematic cross-section of a NC FGM device. The use of an NC floating gate can significantly improve the degree of non-volatility and charge retention time due to the effects of Coulomb blockade, QC [215], and the reduction in charge leakage from isolated NCs through the weak spots in the TO [9]. NC FGM devices using Si NCs were reported by Numonyx for a 4 MB NOR flash [216] and Freescale Semiconductor for a 128 kB NOR memory in the 90 nm technology node in 2008 [217]. To increase the storage density, CEA-Leti company reported the dual layer of Si NC based NFGM devices in 2012 [218]. This suggests that the NC FGM devices can play a stimulating role in driving the consumer memory market in near future.

The NCs serve as the charge storage nodes. The required information can be stored digitally, in the form of ‘0’ or ‘1’ memory states, by injecting charges ‘in’ or removing ‘out’ of the tiny NCs, as shown in figure 20(a). The drain current can be read at V_{read} which is much lower than the programming voltage. The ‘write’ and ‘erase’ mechanisms for a NC memory device are illustrated schematically in figures 20(b) and (c). During the write process, a positive gate voltage is applied to the control gate to inject electrons from the inversion layer into the floating gate containing isolated NCs. The application of a reverse bias causes the reverse tunnelling of electrons into the channel or the accumulation-layer holes to tunnel into the NC. This is known as the erase process, which is schematically shown in figure 20(c). Several tunnelling mechanisms, namely F–N tunnelling, channel hot electron injection (CHEI) and direct tunnelling, are responsible during the programming

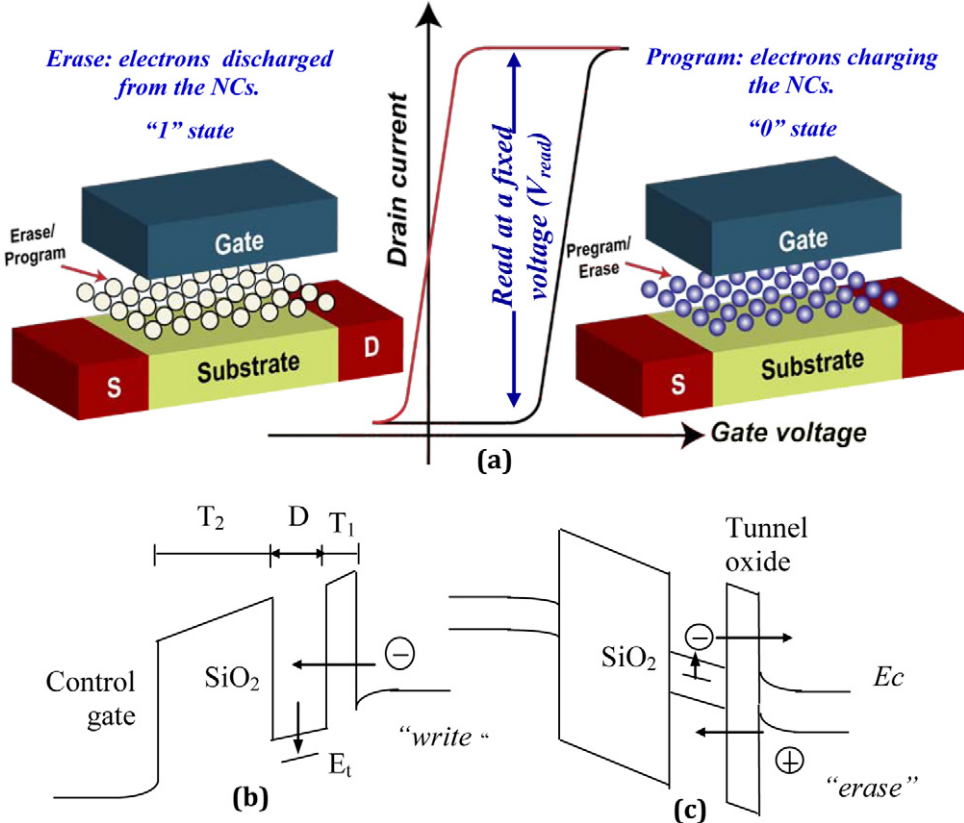


Figure 20. (a) Schematic of the program and erase operation in a NC FGM device. A schematic band diagram illustrating (b) write and (c) erase processes in a Si NC memory device.

operation. The time-dependent tunnelling current density between the two-dimensional electron gas (2DEG) and the NC during the write process can be expressed as [219]

$$J(t) = e \sum_{i,j} g_i \int_{E \geq E_{CN}} P(E) f_j(E) \rho_i(E) f(E) dE, \quad (18)$$

where $P(E)$ is the transmission probability across the tunnel oxide, calculated with the Wentzel–Kramers–Brillouin (WKB) approximation; i is the index for two degenerate valleys (total six valleys) of the conduction band; j is the index of sub-band for each conduction band valley; $\rho_i(E)$ is the density of states for each valley; g_i is the degeneracy for two degenerate valleys and E_{CN} is the conduction band edge in NCs. The tunnelling current is therefore time-dependent since the electrical field across the tunnel oxide depends on the injected charges in the NC. The NC potential is raised by the electrostatic charging energy e^2/C for each tunnelled electron.

In a conventional silicon oxide gate, the cells cannot be scaled down easily because of the trade-off between the thickness of the TO and the charge retention time. The use of a physically thicker high permittivity (high- k) oxide ensures good retention characteristics. On the other hand, thin tunnelling barriers due to the low equivalent oxide thickness (EOT) allow high currents across the TO at low control gate voltages during programming and erasing cycles. The high- k film as a blocking oxide also has a great impact on enhancing the electron injection from the Si substrate under program and on enhancing the hole injection under erase conditions. This

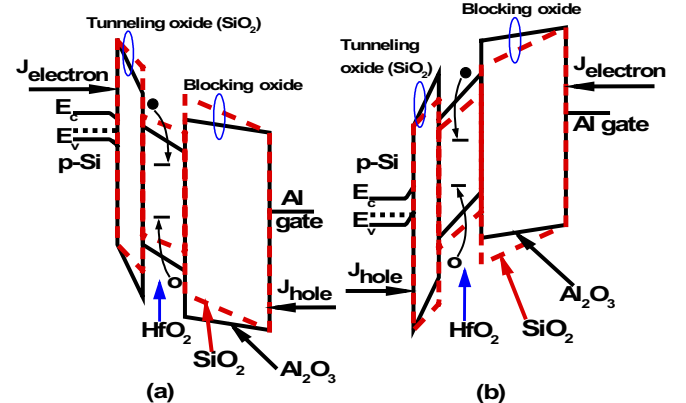


Figure 21. Schematic energy band diagrams of p-Si/SiO₂/HfO₂/Al₂O₃/Al (solid line) and p-Si/SiO₂/HfO₂/SiO₂/Al (dashed line) memory structures under (a) program and (b) erase modes [220].

could be explained by the schematic energy band diagram shown in figure 21 using a p-Si/SiO₂/HfO₂/Al₂O₃/Al memory structure. Under the programming condition, assuming a uniform trap distribution in the high- k HfO₂ films, the charge centroid will be approached at half the HfO₂ film thickness [25] and the flat band voltage shift (ΔV_{FB}) can be simplified as

$$\Delta V_{FB} = \frac{Q_{HfO_2}}{\varepsilon_0} \left[\frac{d_{BO}}{\varepsilon_{BO}} + \frac{d_{HfO_2}}{2\varepsilon_{HfO_2}} \right], \quad (19)$$

where Q_{HfO_2} is the amount of trapped charges per unit area in HfO₂ films. ε_{HfO_2} and ε_{BO} are the relative permittivities

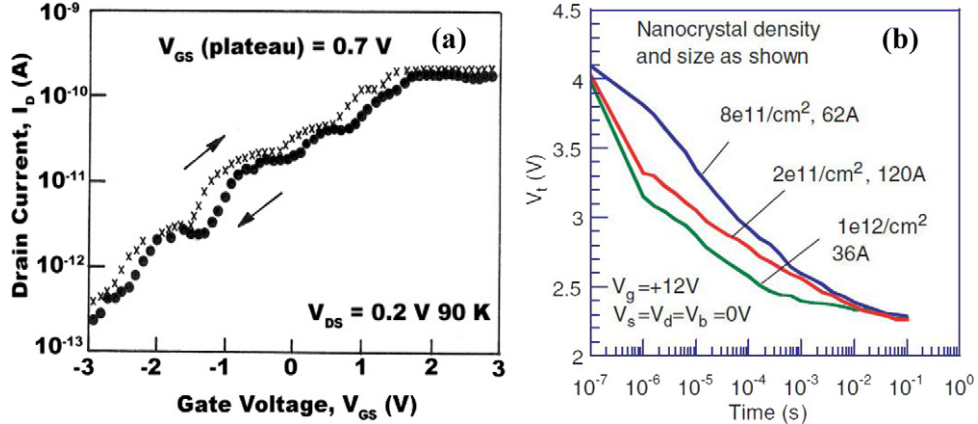


Figure 22. (a) Current–voltage characteristics for Si NC memory showing single electron nature. (Reprinted with permission from Springer: [222], copyright 2000. (b) Reported results on the influence of Si NC density and size on the FN erase speed. (Reprinted with permission from Elsevier Ltd.: [288], copyright 2005).

of the trapping oxide (HfO_2) and the blocking oxide (Al_2O_3), respectively. d_{TO} and d_{BO} are the thicknesses of the trapping oxide (HfO_2) and the blocking oxide (Al_2O_3), respectively, and ϵ_0 is the permittivity of free space. The capacitance-equivalent thickness (CET) of the $\text{SiO}_2/\text{HfO}_2/\text{Al}_2\text{O}_3$ stack dielectrics can be written as [220]

$$d_{\text{eff}} = d_{\text{TO}} + \frac{\epsilon_{\text{TO}}}{\epsilon_{\text{HfO}_2}} d_{\text{HfO}_2} + \frac{\epsilon_{\text{TO}}}{\epsilon_{\text{BO}}} d_{\text{BO}}, \quad (20)$$

where ϵ_{TO} is the relative permittivity and d_{TO} is the thickness of TO (SiO_2). The electric fields across TO (E_{TO}) and blocking oxide (E_{BO}) under the erase mode [220] can be expressed by

$$E_{\text{TO}} = \frac{|V_g| - \phi_{\text{ms}} - \Psi_s - \Delta V_{\text{FB}}}{d_{\text{eff}}} \quad (21)$$

$$E_{\text{BO}} = \left[E_{\text{TO}} + \frac{Q_{\text{HfO}_2}}{\epsilon_0 \cdot \epsilon_{\text{TO}}} \right] \cdot \frac{\epsilon_{\text{TO}}}{\epsilon_{\text{BO}}}, \quad (22)$$

where V_g is the applied gate voltage, ϕ_{ms} is the work function difference between the gate electrode and the p-Si substrate, and ψ_s is the surface potential. Relative permittivities of SiO_2 , HfO_2 and Al_2O_3 films are found to be approximately 3.9, 17 and 8, respectively [220]. For example, in the case of a V_g of 15 V, the electric field across the TO (E_{TO}) is $\sim 14 \text{ MV cm}^{-1}$ and that across the Al_2O_3 blocking oxide (E_{BO}) is $\sim 7.7 \text{ MV cm}^{-1}$, while E_{TO} is $\sim 8.3 \text{ MV cm}^{-1}$ and E_{BO} is $\sim 10 \text{ MV cm}^{-1}$ for the SiO_2 blocking oxide. Therefore, the electric field across TO is very high and that across BO is very low, if one can use Al_2O_3 as a blocking oxide instead of the SiO_2 one. The larger relative permittivity of a trapping layer (HfO_2) and blocking oxide (Al_2O_3) leads to larger difference of E_{TO} and E_{BO} . The calculated energy band diagram on p-Si/ $\text{SiO}_2/\text{HfO}_2/\text{Al}_2\text{O}_3/\text{Al}$ (solid line) and p-Si/ $\text{SiO}_2/\text{HfO}_2/\text{SiO}_2/\text{Al}$ (dashed line) structures under the program/erase mode is shown in figure 21. Under the program mode, electron current (J_{electron}) from the Si conduction layer can be enhanced without any concern of hole current (J_{hole}) injection from the high- k gate electrode. Under the erase mode, J_{hole} from the Si conduction layer can be enhanced and the electron current from the gate electrode can be suppressed

using high- k Al_2O_3 as a blocking oxide. To obtain high program/erase speed, the difference $J_{\text{electron}} - J_{\text{hole}}$ should be high. This suggests that the back tunnelling currents (J_{hole} under the program mode and J_{electron} under the erase mode) can be suppressed by using both large barrier height and large relative permittivity of the high- k blocking oxide. The following sections review a detailed study of the improvement in memory performances using Si, Ge, metal and high- k NC based floating gate structures.

9.1. Si NC memory

The memory devices first demonstrated by Tiwari *et al* [45] are based on a structure with floating islands of Si NCs embedded in the gate oxide. The device used direct tunnelling of electrons from the channel or source/drain, which are stored in the NCs. By controlled charge injection into floating gate NCs through the tunnel barrier, the threshold voltage of the memory devices can be altered. Four features [45] that are crucial for the scaling of these devices to achieve low-voltage, single-electron operation at room temperature are as follows:

- (i) the NC dimensions should be small enough to increase the energy level spacing by QC and the Coulomb blockade;
- (ii) a thin tunnel oxide is preferable to allow direct tunnelling for increase in speed;
- (iii) the control oxide has to be thicker to prevent gate-to-dot and dot-to-dot tunnelling;
- (iv) the device needs to have low interface state densities to reduce offset charges.

Drain current versus gate voltage characteristics of reported MOSFETs with a silicon NC floating gate show hysteresis and current bumps, due to charging and discharging of the quantum dots. Thereafter, several MOSFET memory devices with a threshold voltage shift ranging from 0.25 V to 3.0 V have been demonstrated [45, 221]. A step-like current–voltage characteristic of a Si quantum-dot memory device is shown in figure 22(a), where steps in the drain current correspond to single electron storage in Si dots [222]. There is a strong influence of the traps on the charge storage characteristics in

Si NC memory devices [215]. The role of interface states and deep traps in SiO_2 /nanocrystalline Si (nc-Si)/ SiO_2 devices has been thoroughly examined [55] using temperature- and frequency-dependent electrical properties. Si NC memory devices always encounter a trade-off between the operation speed and the retention time. Different methods [223–225] have been proposed to solve this problem. An increase in retention time by two orders of magnitude has been achieved [223] by fabricating a self-aligned doubly stacked Si NC memory device. The charge leakage between the upper dots and the channel can be suppressed exponentially by the energy barrier due to the QC and Coulomb blockade in the lower dot. This resulted in a dramatic improvement of the charge retention time by reducing the dot size. As compared with the conventional flash memory with the program/erase process dominated by the F–N tunnelling, the Si NC flash memory provides faster operational speed by at least several orders of magnitude due to the direct tunnelling mechanism. The total capacitance for a typical Si NC memory device is of the order of 10^{-16} F and the tunnelling resistance (R_t) is about $10^8 \Omega$, resulting in a programming/erasing time of the order of 10^{-8} s, in the direct tunnelling regime [226]. A junction-assisted programming scheme [227] for Si NC memory devices with improved performance has also been reported. Figure 22(b) shows the reported results on the influence of Si NC density and size on the FN erase speed [228]. The influence of NC size on the transport properties has also been discussed in [229]. The increase in energy levels in smaller NCs results in faster erase. Researchers have also reported few-electron [230] and single-electron [42–44] memories based on NC floating gate structures.

9.2. Ge NC memory

As compared with Si, Ge NCs embedded in oxides offer improved charge retention characteristics due to smaller band gap, which provide a higher confinement barrier for retention mode and a smaller barrier for program and erase modes. However, because of the low evaporation temperature and the difference in surface energy with respect to the oxide, the fabrication of Ge NCs on insulators is much more challenging. Self-assembling [31, 47, 231, 232] and growth [233, 234] of Ge NCs embedded in SiO_2 layer have successfully been implemented. The performance of such a memory device is very sensitive to the thickness uniformity of tunnel oxides and the characteristics of NCs in terms of size, shape, density, crystallinity, orientation, spatial distribution, etc. After the first demonstration [231] of high-speed Ge NC memory devices with a low programming voltage, Ge/Si hetero- [235] and core–shell NC structures [236] have been proposed for further scaling and to improve the NC–insulator interface quality, resulting in better memory performance characteristics.

9.2.1. Ge NCs with SiO_2 as a TO. Most of the work on FGM has focused on Ge NCs embedded in an SiO_2 matrix [31, 47, 231–233, 237–240]. High-frequency capacitance–voltage (C – V) characteristics of rf-sputter-deposited SiO_2 /SiGe/ SiO_2 trilayer samples annealed at 800°C ,

900°C and 1000°C with Ge NCs size of 2.5 nm, 5.3 nm and 10.0 nm, respectively, were investigated. An anti-clockwise hysteresis characteristic indicated the net electron trapping in Ge NCs embedded in the oxide and sandwiched between tunnelling and cap oxides [31]. The increase in hysteresis width, a figure of merit of stored charge density, on post-deposition annealing at higher annealing temperatures was attributed to the improved crystallinity of Ge NCs and the reduction in defects/traps at the interfaces.

Ge NCs as floating gates have been prepared by co-sputtering [31, 47, 57, 241] with dielectric mixture layers, ion implantation [9] and other deposition techniques [242, 243]. However, these processes yield reproducibility far from the desired one required for device integration [55]. Lattice-mismatched SK mode has been used to produce Ge islands of various shapes and sizes on oxide-free Si substrates using molecular beam epitaxy (MBE) [4, 57] and CVD [243]. However, there are only a few studies on the growth of Ge NCs on thin oxide of Si, which could be used as a TO for NC FGM devices [243]. Different sized Ge NCs have been deposited directly on a thin SiO_2 layer by solid source MBE [244] at varying growth temperatures (400, 500 and 550°C). Figure 23(a) represents the high-frequency (1 MHz) capacitance–voltage (C – V) hysteresis behaviour of the MOS capacitors consisting of Ge NCs sandwiched between a thin (4 nm) tunnelling SiO_2 layer and a relatively thick (25 nm) capping Al_2O_3 layer grown on p-Si. An anti-clockwise hysteresis in sweeping the gate voltage is observed indicating net electron trapping in Ge NCs. Large memory windows of hysteresis width 7.23 V, 4.08 V and 5.56 V are observed for the devices for Ge NCs grown at temperatures of 400°C , 500°C and 550°C , respectively, for a voltage sweep of ± 8 V. Table 3 shows the size distribution and stored charge density in MOS capacitors with embedded Ge NCs. Although capacitance–voltage measurement has been widely studied to obtain device characteristics due to the ease of experimental setup and data analysis, the conductance–voltage (G – V) measurement is a relatively sensitive method and can provide further insights into the electrical operation of the devices. The frequency-dependent capacitance and conductance measurements are shown in figure 23(b) for the 550°C growth temperature sample in the frequency range from 50 kHz to 1 MHz for ± 8 V sweep voltage. Nearly a constant hysteresis width in C – V curve and nearly constant FWHM of the conductance peak in the G – V characteristics (figure 23(b)) are observed in the measured frequency range. This indicates that the hysteresis and the conductance peak have the same origin [244] in the above samples, where the contribution from interface traps is negligible. However, a small conspicuous shift in the conductance peak with frequency is observed in G – V measurements. This can be explained by the fact that the conductance is related directly to the energy loss during the capture and emission of carriers by Ge NCs [55].

9.2.2. Ge NCs in high- k oxide matrix. As discussed in figure 21, the vertical scaling and charge retention properties of Ge NC based non-volatile memory devices could be improved by using a high- k oxide material with a large barrier height

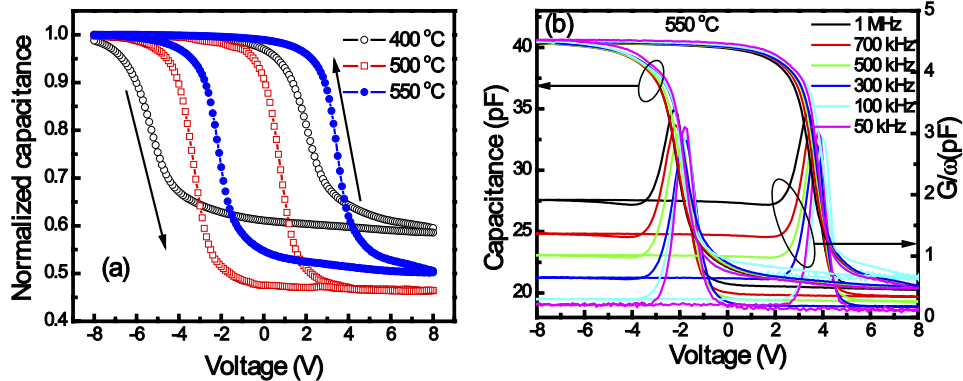


Figure 23. Room-temperature electrical properties of the MOS structures using Ge NCs grown directly on a tunnel oxide by MBE deposition. (a) Capacitance–voltage hysteresis behaviour V with different Ge NC sizes for a voltage sweep of ± 8 , and (b) frequency-dependent C – V and G – V characteristics for the Ge NCs grown at $550\text{ }^\circ\text{C}$.

Table 3. Size distribution and charge storage density for the Ge NC memory devices directly grown on TO using MBE.

| Sample | NC size distribution | | Charge storage density | | |
|--------|----------------------|------------------|--------------------------|------------------------|--------|
| | Height (nm) | Diameter (nm) | Density (cm $^{-2}$) | Total (cm $^{-2}$) | per NC |
| 400 °C | 4.5 | 08.5 | 9.70×10^{11} | 1.27×10^{13} | 13 |
| 500 °C | 7.6 | 15.0 | 2.13×10^{11} | 6.82×10^{12} | 32 |
| 550 °C | 7.8 | 21.4 | 0.71×10^{11} | 8.78×10 | 124 |

such as Al_2O_3 [220]. Alumina exhibits high thermal stability and remains in the amorphous phase even after annealing at $>1000\text{ }^\circ\text{C}$ [245]. High- k Al_2O_3 with a band gap of 6.8 eV has great potential as a blocking oxide to enhance the electron injection from the Si substrate under the program condition and the hole injection under the erase condition [220, 234]. Ge NCs embedded in Hf-based dielectrics, one of the attractive and promising matrices, have been studied only recently [56, 58, 85, 119, 246, 247]. The leakage current of HfO_2 is several orders of magnitude smaller than that of SiO_2 for the same EOT [248], resulting in superior data retention behaviour. On the other hand, HfO_2 can provide a larger tunnelling current than SiO_2 during program operation, due to the lower electron barrier height of HfO_2 (1.2 eV) [249] as compared with SiO_2 (3.1 eV). Figure 24(a) shows a typical cross-sectional TEM micrograph of the $\text{HfO}_2/\text{Ge NCs}+\text{HfO}_2/\text{HfO}_2$ trilayer structure prepared by rf sputtering. The high-resolution micrograph showing the lattice fringes reveals the formation of nearly spherical-shaped and isolated Ge NCs of diameter in the range 5.0–8.0 nm. The formation of a Hf-silicate interfacial layer of 2 nm thick, which may also act as a tunnel dielectric, is also evident in the micrograph. Figure 24(b) shows the high-frequency (100 kHz) C – V hysteresis curves for $800\text{ }^\circ\text{C}$ and $900\text{ }^\circ\text{C}$ annealed Ge NC embedded trilayer memory capacitors for a sweep voltage of ± 5.0 V. An anti-clockwise hysteresis characteristic is observed in both the samples indicating net electron trapping in the Ge-NC embedded sandwiched structure. A large memory window of 3.39 V and 2.02 V, as compared with that of 0.12 V in the control sample, is observed for the $800\text{ }^\circ\text{C}$ and $900\text{ }^\circ\text{C}$ annealed samples, respectively. Figure 24(c) shows the retention characteristics

of HfO_2 -embedded Ge NC non-volatile memory devices at room temperature. The initial memory window widths of the $800\text{ }^\circ\text{C}$ and $900\text{ }^\circ\text{C}$ devices are 2.02 V and 3.39 V, respectively. After 10 years of retention, the memory windows of the $800\text{ }^\circ\text{C}$ and $900\text{ }^\circ\text{C}$ annealed sample are estimated to be 0.63 V and 2.02 V, respectively at room temperature giving rise to charge losses of 40% and 68%. This charge loss mechanism can be attributed to two processes: (i) initial fast decay, due to the lateral charge loss and the Coulomb repulsion between electrons confined in NCs [250], and (ii) slow decay, attributed to the leakage via the tunnelling barrier [251]. It is seen that for the higher temperature annealed sample, the initial fast decay is suppressed due to the complete isolation of Ge NCs [251]. Figure 24(d) shows the endurance characteristics of the Ge NCs embedded in HfO_2 memory devices for a sweep voltage of ± 5.0 V. After 10^2 write/erase cycles with ± 5 V bias, there is only 0.35 V shift of V_{FB} , which is believed to be due to the contribution from interface states. Thereafter, for up to 10^3 write/erase cycles, no further degradation is observed.

9.2.3. Tunnel barrier engineering in Ge NC based memory devices. The scaling of thickness of tunnel oxide for non-volatile memory devices plays a crucial role, if ten-year data retention is an essential requirement. This requirement limits further improvement of device performance in terms of programming speed and operating voltages. A promising solution for tunnel oxide scaling is tunnel barrier engineering (TBE) [56, 252–254], which uses multiple dielectric stacks to enhance the field sensitivity. This approach allows shorter writing/erasing times and/or lower operating voltages than the single tunnel oxide, without altering the ten-year data retention constraint. The creation of asymmetric energy barrier in the TO, which is dependent on the memory status, can be useful for TBE. A numerical model [254] to assess potential layered tunnel barrier materials and a nitride–oxide–nitride structure with an adjustable barrier height has been proposed [252]. Simulations and experimental results of a novel variable oxide thickness (VARIOT) structured tunnel oxide [253] showed that a larger injected gate current density is possible for the memory devices as compared with the one with only a single layered tunnel oxide [56, 144, 253].

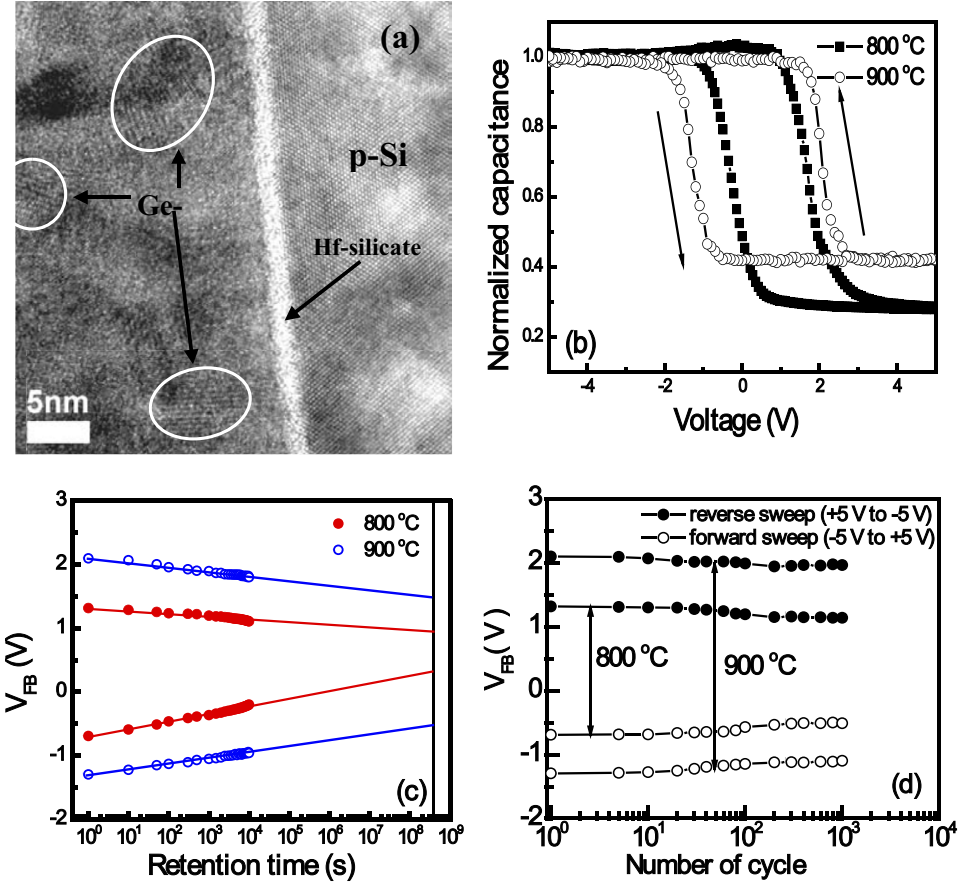


Figure 24. (a) Cross-sectional high-resolution TEM micrograph showing Ge NCs in an HfO_2 matrix; and (b) high-frequency (100 kHz) capacitance–voltage, (c) retention and (d) endurance characteristics for the 800 °C and 900 °C annealed $\text{HfO}_2/\text{Ge NCs}+\text{HfO}_2/\text{HfO}_2$ trilayer memory capacitors [110].

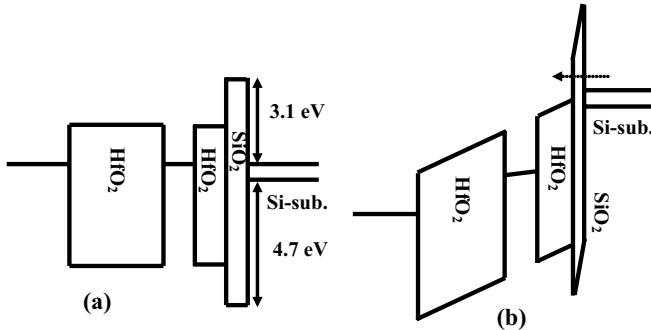


Figure 25. Schematic energy band diagram of the VARIOT memory device at (a) flatband condition and (b) under the program mode [144].

Figures 25(a) and (b) show the band diagrams including the valence band of the VARIOT structure in the flatband condition and under the program mode, respectively. During the writing process, when a sufficient voltage occurs across the SiO_2 film, shown figure 25(b), it forces the conduction band edge of the Si substrate to be higher than the conduction band edge of HfO_2 . The tunnelling current is then mainly determined by a strong direct tunnelling contribution. On the other hand, the tunnelling current density of a memory cell with a single-layer tunnel HfO_2 is limited by a much smaller F–N current. Therefore, the writing speed of the memory

with a VARIOT structure is faster than that of a single HfO_2 tunnel barrier. Due to the asymmetric stack structure of the tunnelling barrier of the VARIOT device, the erasing speed of the VARIOT device is not as fast as its writing speed.

Figure 26(a) shows the C – V characteristics of VARIOT ($\text{HfO}_2/\text{Ge NCs}+\text{HfO}_2/\text{HfO}_2/\text{SiO}_2/\text{p-Si}$) memory devices annealed at 800 and 900 °C for ± 6 V sweep voltage. High-frequency C – V curves show large flat-band voltage shift during the forward and reverse sweeping. This is attributed to the larger gate capacitive coupling factor resulting from the higher dielectric constant HfO_2 cap layer. Since a higher electric field is channelled to the NCs from the applied gate bias, this results in more NCs being active in the conduction process. Maximum flat band voltage shifts of 4.42 and 4.67 V obtained for the 800 and 900 °C annealed devices give rise to stored charge densities, N_{charge} , of $1.3 \times 10^{13} \text{ cm}^{-2}$ and $1.7 \times 10^{13} \text{ cm}^{-2}$, respectively. Figure 26(b) shows the charge retention characteristics of the Ge NC based VARIOT memory capacitor. The memory windows of the 900 °C and 800 °C annealed devices are estimated to be 4.09 V and 3.74 V, respectively. After 10 years of retention at room temperature, the corresponding charge losses of the memory are estimated to be 13% and 16%, respectively. This result indicates that SiO_2 in the VARIOT structure plays a very important role because of the higher band offset during the retention condition. Due to the large memory window and low charge loss of the Ge NC memory device with a VARIOT

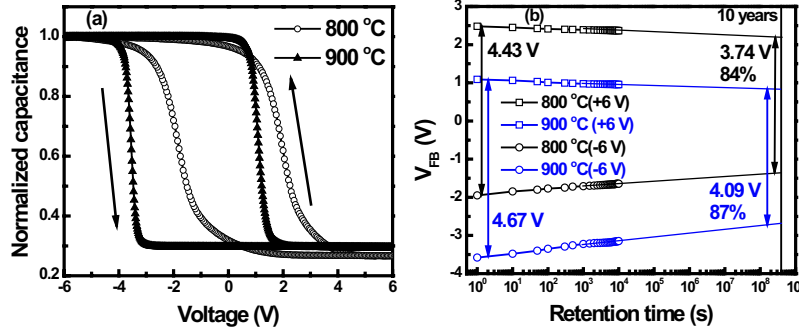


Figure 26. (a) High-frequency (1 MHz) capacitance–voltage and (b) retention characteristics of the VARIOT memory devices annealed at 800 and 900 °C.

tunnelling barrier, it can be used in future high-density and scaled flash memory device applications.

10. Metal NC based memory devices

10.0.4. Electric field enhancement in metal NCs. To achieve optimized device performance at a low voltage operation with enhanced program/erase speed without degrading the retention property, one possible way is to engineer the depth of the potential well [48, 255]. This can provide a sufficiently large energy band offset (EBO) between the TO layer and the storage nodes. Metal NCs are the most obvious choice for this kind of deep quantum well due to their high available work function values [48]. The EBO of the DQW structure is very much tunable with the modulation of WF for the metal NCs. Furthermore, the electric field on the surface of the metallic NCs is much higher than that of the semiconductor [256]. Considering the NC FGM devices, the tangential electric field (E_θ) could be written as

$$E_\theta = -E_0 \left\{ 1 - \frac{a^3}{r^3} \left(\frac{\epsilon_{NC} - \epsilon}{\epsilon_{NC} + 2\epsilon} \right) \right\} \sin \theta, \quad (23)$$

where E_0 is the electric field set by the parallel plates without the NCs, ' a ' is the radius of the conductor or semiconductor NC, ' r ' is any arbitrary point (figure 27(a)), ' ϵ ' is trap-free dielectric permittivity, ' ϵ_{NC} ' is the NC permittivity, and ' θ ' is the angle between r and E_0 . It is well known that the Debye length is smaller than 0.1 nm and $\epsilon_{NC} \rightarrow \infty$ for most of the metals. Thus, for example, at the centre of the Au NC, where $r = a$, the value of E_θ has to be zero. Figure 27(b) shows the 3D model geometry. The electric field is predicted to be enhanced on the surface of the metal NCs, as shown in figure 27(c), which can affect the electron tunnelling probability. Due to this electric field enhancement, a significant tunnelling is possible at a lower gate voltage (and hence larger memory window) for metal NC FGM devices. In a similar way, double-layer metal NCs could also be charged by the enhancement of electric field [257]. On the other hand, it is clearly understood that the electric field for the semiconductor NCs depends on the dielectric constant ratio, which allows the electric field inside the NCs. Thus, the program/erase for the metal NCs is more efficient than that of the semiconductor ones. However, the synthesis of uniform and small-sized metal NCs, keeping all aspects on the right ways, is a critical task.

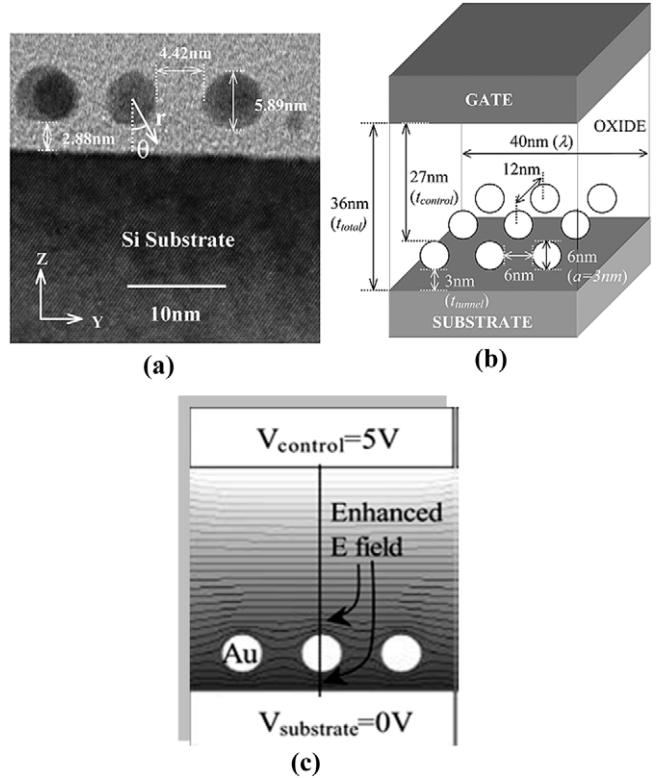


Figure 27. (a) Cross-sectional STEM image of an Au NC memory device. The Au NCs were embedded in the gate oxide. (b) Corresponding 3D model geometry. The NCs have radius ' a ' and the stored charge Q_0 , and embedded in a uniform electric field of E_0 by the parallel plate. (c) The potential contour of Au NC memories is shown showing the electric field enhancement on the Au NC surface. (Reprinted with permission from IEEE: [256], copyright 2005).

10.0.5. Characteristics of metal NC memory devices. Metal NCs can be formed using three conventional methods; (i) chemical, (ii) precipitation and (iii) thermal treatment of a thin metal film [258–262]. It is well known that, due to the lower Gibbs free energy (ΔG) value, a lower temperature is required for the formation of isolated metal NCs along with the perturbation from a thin metal nanolayer. The minimization of surface energy and the dispersion force between the top and bottom interfaces of the thin layer would help in stabilizing the layer. Therefore, the final geometry depends on the balance between these driving forces. Due to the well controllable

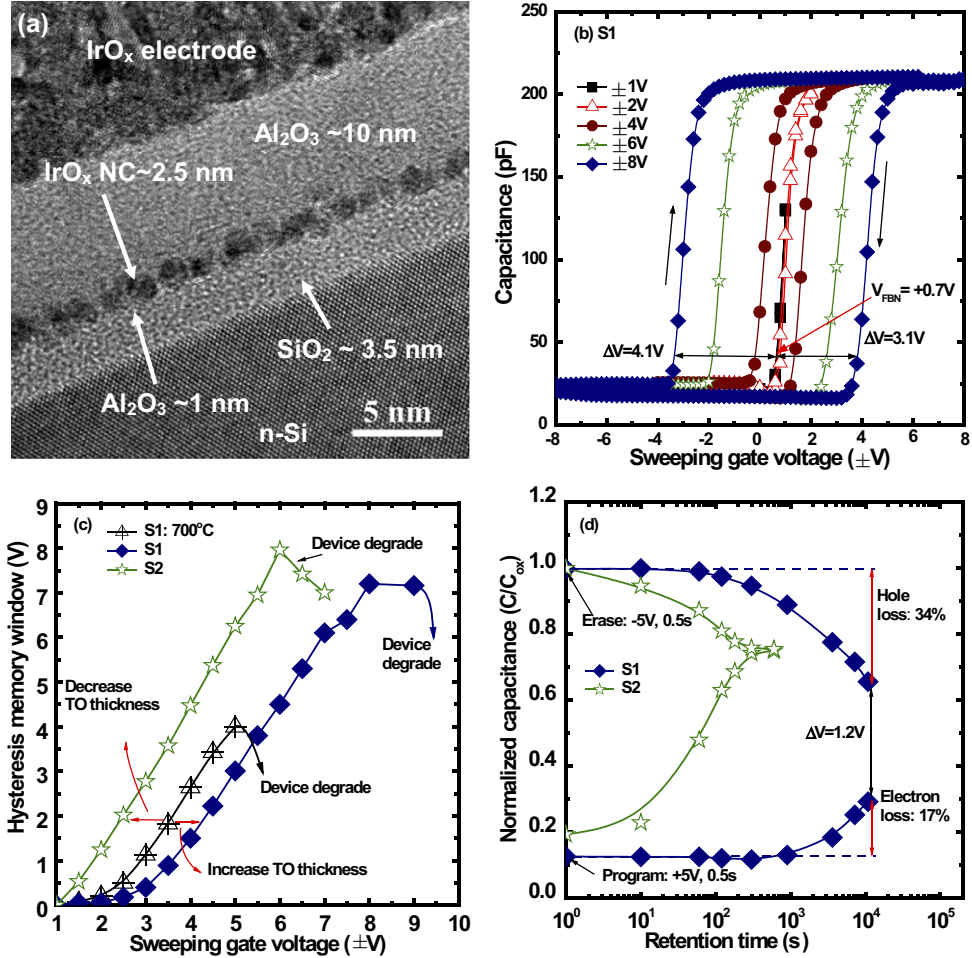


Figure 28. (a) Cross-sectional HRTEM image of a n-Si/SiO₂/Al₂O₃/IrO_x NC/Al₂O₃/IrO_x structure. (b) C–V hysteresis characteristics of the IrO_x NC memory capacitor. (c) Flat-band voltage shift versus sweeping gate voltage characteristics. (d) Data retention characteristics of the S1 and S2 memory capacitors [271].

thermal budget, lower formation temperature based metal NCs are preferable for standard CMOS processes [261]. Several experimental methods such as sputtering, atomic layer deposition (ALD) and e-beam evaporation have been employed towards this evolution of metal NC based FGM devices. Different NCs such as Al, Au, Co, Ni, TiN, NiSi, Ru, RuO_x and IrO₂ have been reported by many research groups [49–54, 263–270]. Even though an array of metal NCs can be formed on TO/Si, the degradation of thin oxide needs to be considered for practical nanoscale non-volatile memory applications.

The thickness uniformity, quality and energy gap of the TO are the major issues to achieve high-reliability memory devices. To investigate the TO quality, IrO_x metal nanolayers with nominal thicknesses of ~1.5 nm (sample: S1) and 2.5 nm (sample: S2) are fabricated [271]. Figure 28(a) shows the cross-sectional HRTEM image of the IrO_x NC memory capacitor (S1). The thickness of the TO (SiO₂+Al₂O₃) layer is about 4.5 nm. Isolated IrO_x NCs with a thickness of 2.5 nm are observed clearly. The thickness of the IrO_x NC layer is increased over that of the as-deposited one (2.5 nm versus 1.5 nm) owing to the formation of NCs. The thickness of the blocking oxide (BO) of the high-*k* Al₂O₃ film is about 10 nm. Figure 28(b) shows the C–V hysteresis characteristics

of the n-Si/SiO₂/Al₂O₃/IrO_x/Al₂O₃/IrO_x memory capacitor for sample S1. The neutral flat-band voltage (V_{FBN}) is +0.7 V. The hysteresis memory windows (ΔV s) are ~3 V and 7.2 V under the sweeping gate voltages of ±5 V and ±8 V, respectively. The electron and hole trapping behaviour of the IrO_x NCs can be explained as follows. The Gibbs free energies of the SiO₂, Al₂O₃ and IrO₂ films are $-699.88 \text{ kJ mol}^{-1}$, $-869.25 \text{ kJ mol}^{-1}$ and $-35.5 \text{ kJ mol}^{-1}$ at 900 °C, respectively. So the high-*k* Al₂O₃ film can be easily oxidized. The core region of the IrO_x NCs is found to be Ir-rich with oxygen vacancy (i.e. positive-type defects) and the annular region of the IrO_x NCs is Al-rich with oxygen gathering (i.e. negative-type defects). So the electrons can be trapped inside (core region) the NCs and the holes can be trapped on the boundary (annular region) of the NCs. The hysteresis memory window increases with the sweeping gate voltage (figure 28(c)). For comparison, the S1 capacitor with rapid thermal annealing (RTA) at 700 °C (S1:700) is used. To obtain a 1 V memory window, a sweeping voltage of ~3 V is necessary for the S1:700 memory capacitor. To obtain the same memory window, sweeping voltages of ±3.6 V and ±1.8 V are needed, respectively, for S1 and S2 capacitors annealed at 900 °C. This is due to the increase in TO thickness in the former. The S1:700 memory device is permanently degraded after ±5 V sweep,

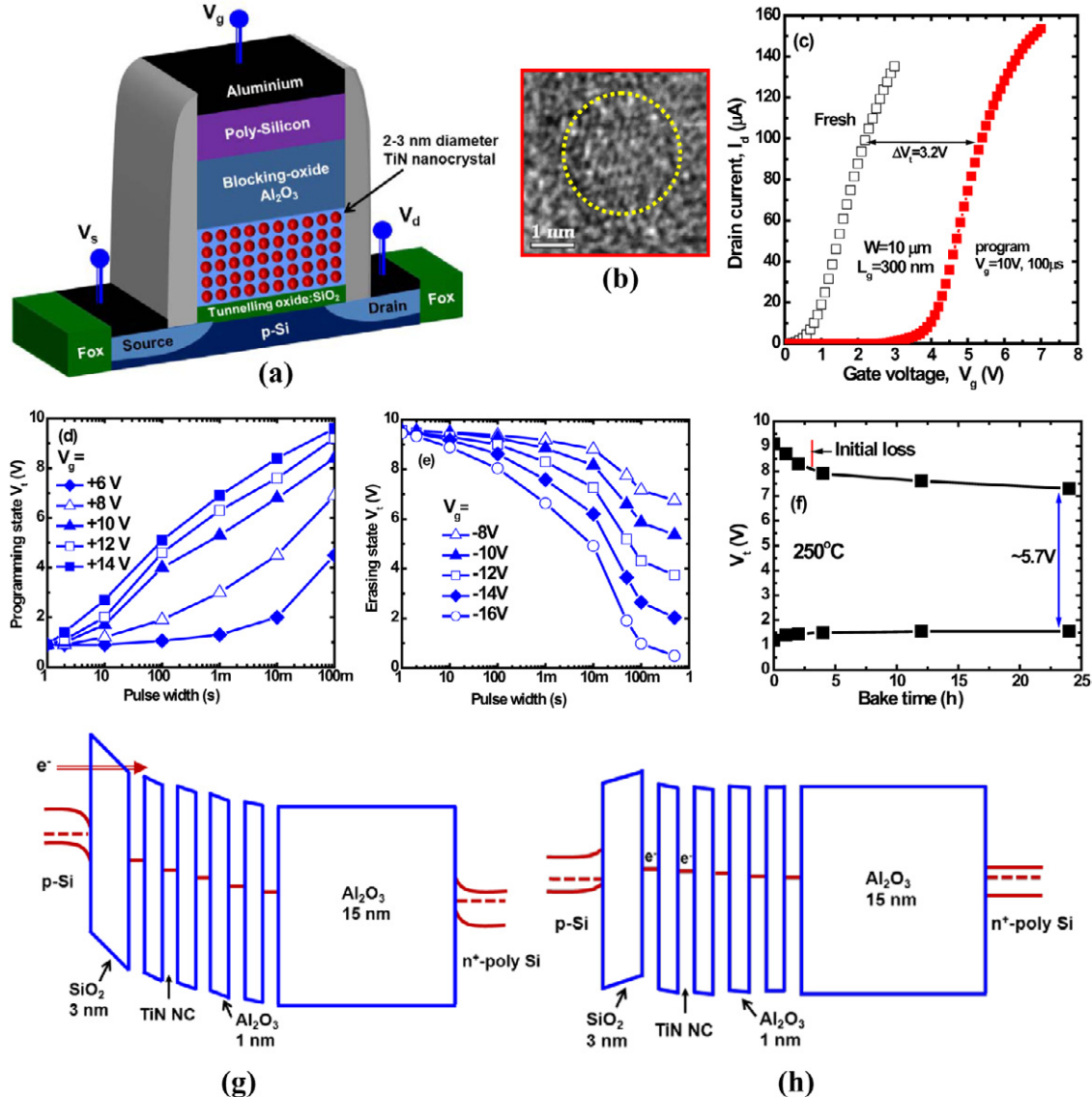


Figure 29. (a) Schematic view of the multiple TiN NC memory device. (b) High-resolution image of a single TiN NC [54]. (c) Typical $I_d - V_g$ characteristics of the TiN NC MOSFET device. (d) Program and (e) erase under FN injections are shown. A large memory window of $\sim 8.8 \text{ V} @ 1 \text{ ms}$ is observed for multilayer TiN NC memory devices ($L_g = 300 \text{ nm}$). (f) Typical charge loss characteristics at 250°C for the memory transistors. Schematic energy band diagrams under (g) programming and (h) retention modes of the multilayer TiN NC flash memory devices.

which may be attributed to some defects in the TO. The S2 memory is degraded at a smaller sweeping voltage than S1, indicating the inferior quality of the TO in the former. This is due to metal migration towards the TO, which shows a smaller TO thickness of the S2 memory during the annealing process. It is suggested that a thin ($\sim 1.5 \text{ nm}$) IrO_x nanolayer may be very useful for future nanoscale charge trapping memory device design. Figure 28(d) shows the retention characteristics for the S1 and S2 memory devices. After 300 s elapsed time, no memory window is observed for S2 owing to the thinner and defective TO. A reasonably high memory window of 1.2 V is observed after an elapsed time of 10^4 s for the S1 devices. The hole loss ($\sim 34\%$) is higher than that of the electron loss of $\sim 17\%$, due to the trapped electrons in the core region and the trapped holes on the NC boundary. This indicates that the holes are closer to the Si substrate than the electrons, making

the tunnelling easier from the trapping layer to the Si substrate. It is suggested that a thinner metal layer ($\sim 1.5 \text{ nm}$) of IrO_x with a high-quality TO is necessary for future low voltage operation nanoscale flash applications.

10.0.6. Multilayer metal NC devices. To achieve lower operating voltage and high performance flash memory devices, several groups reported NC FGM devices using different metal NCs [49, 272–277]. A dual-layer NC memory showed better performance [257] than the single layer NCs. Therefore, the use of multilayer metal NCs is attractive to achieve improved memory devices. For example, we have synthesized tiny TiN NCs with a diameter of $< 3 \text{ nm}$ by ALD after a subsequent annealing treatment at 900°C [54] of TiN (0.5 nm)/ Al_2O_3 (1 nm) nano-laminate layers having five periods. Figure 29(a) shows a schematic view of the MOSFET memory device with

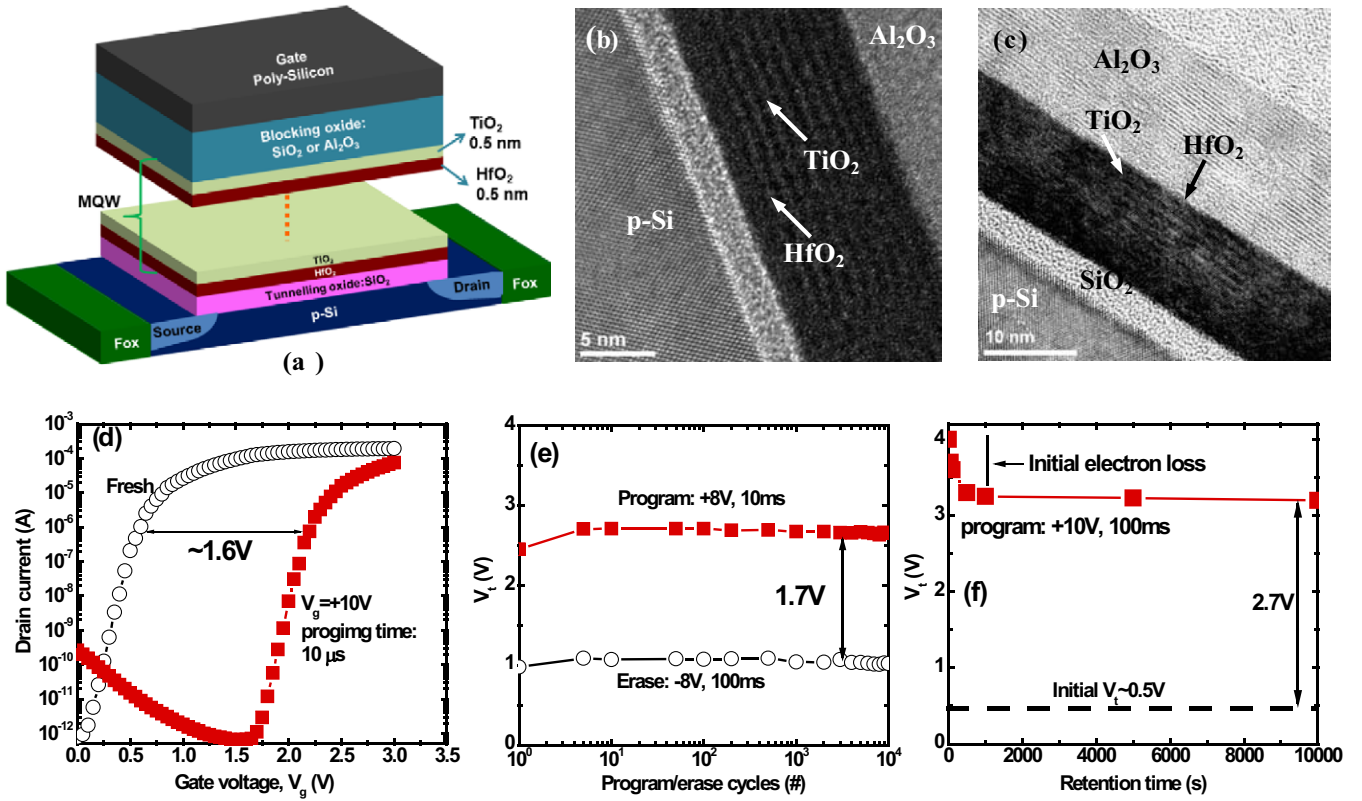


Figure 30. (a) Schematic view of the HfO₂/TiO₂ multilayer potential well flash memory MOSFET device. HRTEM images of 10 periods of (b) as-deposited and (c) post-processed HfO₂(0.5 nm)/TiO₂(0.5 nm) layers [281]. (d) $I_d - V_g$ characteristics of the memory transistor: fresh and after a programming voltage of +10 V with a short pulse width of 10 μ s. (e) Stable endurance characteristics of a multilayer flash memory transistor. (f) Retention characteristics of the HfO₂/TiO₂ multiple well transistors at 25 °C.

multilayer TiN NCs embedded in high- k Al₂O₃ films. The high-resolution TEM image of a single TiN NC showing lattice fringes is presented in figure 29(b). Figure 29(c) shows the drain current versus gate voltage ($I_d - V_g$) characteristics, before and after programming of memory transistors. The thickness of the blocking oxide is \sim 15 nm. A promising memory window (ΔV_t) of \sim 3.2 V under a program voltage (V_g) of +10 V and a pulse width of 100 μ s is observed. The memory window could be enhanced to 8.7 V with a programming voltage of +14 V and a pulse width of 100 ms, as shown in figure 29(d). A memory window of >1 V under a small programming voltage of +8 V and a pulse width of 100 μ s is also observed, which is very useful for low-voltage operation. To erase the memory device (\sim 1 V window), an erasing voltage of $<$ −10 V and a pulse width of 10 ms are necessary (figure 29(e)). Robust data retention with a large memory window of 5.7 V after 24 h baking time at 250 °C is observed (figure 29(f)). Initially, the charge decays rapidly; however, after certain elapsed time a negligible charge loss is observed, which is due to the charge storage in the discrete multilayer TiN NCs. During programming, the electrons can be stored in each layer of the multilayer TiN NCs, as shown in multiple wells in figure 29(g). The stored electrons in the TiN NCs near the Si channel will be lost initially; however, the stored electrons in the potential well at a large distance from the Si channel are retained for a longer time, giving rise to negligible loss even at a temperature of 250 °C (figure 29(h)).

This is in agreement with other reported results [269, 278] on multilayer NCs. Therefore, charge storage in multilayer metal NCs is attractive. Although the performance of the metal NC based FGM devices shows promise, non-uniformity, TO quality, poor isolation of the individual NCs, integration, etc are still the key challenges for future realization of flash memory devices.

11. High- k NC-based memory devices

High- k NCs can also be used as a discrete charge storage node. The high- k NCs can be made from the phase separation at the high-temperature annealing treatment (>900 °C) of mixed oxides. A silicate layer with a thickness of 12 nm amorphous HfSiO_x on a TO layer was deposited by the co-sputtering method with pure Si and pure Hf targets in oxygen gas ambient. The formation of HfO₂ NCs embedded in an SiO₂ matrix has been reported with an average size of 5–8 nm and a density of \sim 1.9 \times 10¹² cm⁻². The mechanism responsible for the formation of HfO₂ NCs is the transformation of hafnium silicate into a phase-separated microstructure by spinodal phase separation after RTA [50].

Flash memory MOSFET devices with enhanced memory performance can be fabricated using multilayers of ultrathin high- k oxides, resembling a multilayer NC memory structure [279–280]. Figure 30(a) shows the schematic view of the multi-well flash memory device using high- k HfO₂/TiO₂

multilayers. The high-*k* HfO₂ film with a thickness of 0.5 nm for each layer is grown by ALD on 3 nm tunnel oxide/Si. The high-*k*TiO₂ film with a thickness of 0.5 nm for each layer could be deposited by plasma-enhanced ALD (PEALD) process forming ten periods of amorphous HfO₂/TiO₂ multilayers. Figure 30(b) shows an HRTEM image of as-deposited high-*k* HfO₂/TiO₂ multilayers showing all isolated layers. After an RTA treatment of 900 °C for 1 min, layers are also distinctly observed in figure 30(c) [281]. It may be noted that the binding energies of Hf–O and Ti–O bonds for HfO₂/TiO₂ multilayers are similar to the pure HfO₂ and TiO₂ films. Therefore, there is almost no inter-diffusion or intermixing between the Hf and Ti atoms in HfO₂/TiO₂ multilayers after the high-temperature annealing treatment giving rise to multiple energy wells. These multiple HfO₂/TiO₂ interfaces can be used as charge trapping centres. Figure 30(d) shows the $I_d - V_g$ characteristics of a multilayer HfO₂/TiO₂ MOSFET memory device. A memory window of 1.6 V is observed under a program voltage (V_g) of +10 V and a small pulse width of 10 μ s. Stable program/erase endurance of $>10^4$ cycles is also observed in figure 30(e), which could be extended to more than 10^6 cycles. Initially, the charge loss is high; however, a negligible charge loss is observed after 10^4 s, as shown in figure 30(f). The initial charge loss takes place for the electrons stored near the Si channel and good data retention is observed due to the electrons stored in multiple interfaces located far away from the channel. Therefore, multiple potential well charge storage memory structures may also be very interesting and useful in future nanoscale non-volatile memory applications.

12. Conclusion

Silicon microphotonics, a technology that combines the integration of photonic components with silicon microelectronic devices, is rapidly evolving. In this paper, we have reviewed the recent advances on the synthesis and characteristics of some group-IV semiconductor (Si and Ge) and metal nanocrystals for futuristic light-emitting and floating gate flash memory devices. The progress made in the last several years to overcome the main bottleneck of the indirect band structure of Si and Ge for efficient light sources using their nanocrystals is discussed. The key features discussed include the effect of QC, exciton binding energy, radiative lifetime, and size on the optical properties of Si and Ge nanocrystals. The attainment of strong visible luminescence at room temperature from nanocrystals embedded in high band oxide matrices make them attractive for future electroluminescent devices. Some of the important challenges for practical applications are to achieve narrow size distribution, an increase in the power efficiency by controlling the injection mechanisms, understanding the role of defects, interfaces and host matrix stress on the emission, to minimize the amorphous content for small-sized clusters, fabrication of multilayer nanocrystals for high-power LEDs etc. On the other hand, rare-earth-doped Si and Ge nanocrystals could be an important platform to design and fabricate LEDs at the communication wavelength (1.5 μ m) by enhanced energy transfer from nanocrystal excitons and resultant excitation of Er³⁺ ions in a transparent and non-centrosymmetric glass matrix for

subsequent emission. These nanocrystals could also be ideal candidates for their applications in Si-based floating gate non-volatile nano-scaled memory devices, making them multifunctional in nature. However, the reliability of tunnel oxides, the mechanism of charge injection (preferably direct tunnelling), and design trade-off in terms of programming voltage, speed and data retention need to be completely understood for their practical applications. Metallic nanocrystals appear attractive on many of the above aspects because of the enhanced electric field on the surface of the NCs and the formation of a deeper potential well. The ease of fabrication of their multilayer stacks in combination with CMOS compatible high-*k* oxides makes them interesting candidates for scaled device technology including novel nanocrystal-based resistive switching memory devices.

Acknowledgments

The authors gratefully acknowledge the contribution of Dr K Das, S Manna, R Alugiri, Dr R K Singha, Professor L Pavesi and Professor A Dhar for many research results presented in the review. The authors are also grateful to Dr C H Lin, Dr P J Tzeng and Dr M J Tsai from the Electronic and Optoelectronic Research Laboratory (EOL), Industrial Technology Research Institute (ITRI), and Dr T Y Wang and Dr J R Yang from National Taiwan University, and Dr P W Li from National Central University, Taiwan, for their research results and experimental contributions to this review paper.

References

- [1] Walters R J, Bourianoff G I and Atwater H A 2005 *Nature Mater.* **4** 143
- [2] Klimov V I, Ivanov S A, Nanda J, Achermann M, Bezel I, McGuire J A and Piryatinski A 2007 *Nature* **447** 441
- [3] Takeoda S, Fuji M and Hayashi S 2000 *Phys. Rev. B* **62** 16820
- [4] Singha R K, Manna S, Das S, Dhar A and Ray S K 2010 *Appl. Phys. Lett.* **96** 233113
- [5] Matthiesen C, Vamivakas A N and Atature M 2012 *Phys. Rev. Lett.* **108** 093602
- [6] Simmons C B et al 2009 *Nano Lett.* **9** 3234
- [7] Klein L J et al 2004 *Appl. Phys. Lett.* **84** 4047
- [8] Shin S J, Jung C S, Park B J, Yoon T K, Lee J J, Kim S J, Choi J B, Takahashi Y and Hasko D G 2010 *Appl. Phys. Lett.* **97** 103101
- [9] Hanafi H I, Tiwari S and Khan I 1996 *IEEE Trans. Electron Devices* **43** 1553
- [10] Shaji N et al 2008 *Nature Phys.* **4** 540
- [11] Sunn X, Liu J, Kimerling L C and Michel J 2009 *Opt. Lett.* **34** 1198
- [12] Liu J, Sun X, Pang D, Wang X, Kimerling L C, Koch T L and Michel J 2007 *Opt. Express* **15** 11272
- [13] Tsybeskov L, Kamenev B V, Baribeau J M and Lockwood J 2006 *IEEE J. Sel. Top. Quantum Electron.* **12** 1579
- [14] Maeda Y, Tsukamoto N, Yazawa Y, Kanemitsu Y and Masumoto Y 1991 *Appl. Phys. Lett.* **59** 3168
- [15] Liao M H, Yu C Y, Guo T H, Lin C H and Liu C W 2006 *IEEE Electron Device Lett.* **27** 4
- [16] Choi W K, Ho Y W, Ng S P and Ng V 2001 *J. Appl. Phys.* **89** 2168
- [17] Lin G R, Lin C J and Kuo H C 2007 *Appl. Phys. Lett.* **91** 93122
- [18] de Boer W D A M, Timmerman D, Dohnalova K, Yassievich I N, Zhang H, Buma W J and Gregorkiewicz T 2010 *Nature Nanotechnol.* **5** 878

- [19] Abstreiter G 1998 Band gaps and light emission in Si/SiGe atomic layer structures *Light Emission in Silicon From Physics to Devices*. Semiconductor and Semimetals vol 49, ed D J Lockwood (San Diego, CA: Academic) pp 37–76, 16, 19, 20
- [20] Presting H, Kibbel H, Jaros M, Turton R M, Menczigar U, Abstreiter G and Grimmeiss H G 1992 *Semicond. Sci. Technol.* **7** 1127
- [21] Menczigar U, Abstreiter G, Olajos J, Grimmeiss H, Kibbel H, Presting H and Kasper E 1993 *Phys. Rev. B* **47** 4099
- [22] Zakharov N D, Talalaev V G, Werner P, Tonkikh A A and Cirlin G E 2003 *Appl. Phys. Lett.* **83** 3084
- [23] Canham L T 1990 *Appl. Phys. Lett.* **57** 1046
- [24] Lu Z H, Lockwood D J and Baribeau J-M 1995 *Nature* **378** 258
- [25] Inokuma T, Wakayama Y, Muramoto T, Aoki R, Kurata Y and Hasegawa S 1998 *J. Appl. Phys.* **83** 2228
- [26] Ledoux G, Guillois O, Porterat D, Reynaud C, Huiskens F, Kohn B and Paillard V 2000 *Phys. Rev. B* **62** 15942
- [27] Pavesi L, Dal Negro L, Mazzoleni C, Franzo G and Friolo F 2000 *Nature* **408** 440
- [28] Zaharias, Freistadt H, Stolze F, Drusdau T P, Rosenbauer M and Stutzmann M 1993 *J. Non-Cryst. Solids* **164** 1089
- [29] Dutta A K 1995 *Appl. Phys. Lett.* **68** 1189
- [30] Paine D C, Caragianis C, Kim T Y, Shigesato Y and Ishahara T 1993 *Appl. Phys. Lett.* **62** 2842
- [31] Das K, NandaGoswami M, Mahapatra R, Kar G S, Dhar A, Acharya H N, Maikap S, Lee J -H and Ray S K 2004 *Appl. Phys. Lett.* **84** 1386
- [32] Zacharias M and Fauchet P M 1997 *Appl. Phys. Lett.* **71** 380
- [33] Min K S, Shcheglov K V, Yang C M, Atwater C A, Brongersma M L and Polman A 1996 *Appl. Phys. Lett.* **68** 2511
- [34] Dehlinger B G, Diehl L, Gennser U, Sigg H, Faist J, Ensslin K, Grutzmacher D and Muller E 2000 *Science* **290** 2277
- [35] Stephen A Lynch *et al* 2006 *IEEE J. Sel. Top. Quantum Electron.* **12** 1570
- [36] Bormann I, Brunner K, Hackenbuchner S, Zandler G, Abstreiter G, Schmult S and Wegscheider W 2002 *Appl. Phys. Lett.* **80** 2260
- [37] Fujii M, Imakita K, Watanabe K and Hayashi S 2004 *J. Appl. Phys.* **95** 272
- [38] Irrera A, Iacona F, Franzò G, Miritello M, Lo Savio R, Eloisa Castagna M, Coffa S and Priolo F 2010 *J. Appl. Phys.* **107** 054302
- [39] Garrido B, García C, Pellegrino P, Navarro-Urrios D, Daldozzo N, Pavesi L, Gourbilleau F and Rizk R 2006 *Appl. Phys. Lett.* **89** 163103
- [40] Kanjilal A, Rebohle L, Baddela N K, Zhou S, Voelkskow M, Skorupa W and Helm M 2009 *Phy. Rev. B* **79** 161302
- [41] Das K, Nagarajan V, NandaGoswami M L, Panda D and Ray S K 2007 *Nanotechnology* **18** 095704
- [42] Tiwari S, Rana F, Chan K, Shi L and Hanafi H 1996 *Appl. Phys. Lett.* **69** 1232
- [43] Guo L, Leobandung E and Chou S Y 1997 *Science* **275** 649
- [44] Wasshuber C, Kosina H and Selberherr S 1998 *IEEE Trans. Electron Devices* **45** 2365
- [45] Tiwari S, Rana F, Chan K, Hanafi H, Wei C and Buchanan D 1995 *Technical Digest of Int. Electron Devices Meeting* p 521
- [46] Blauwe J D *et al* 2000 *IEEE Int. Electron Devices Meeting (IEDM) Technical Digest* p 683
- [47] Choi W K, Chim W K, Heng C L, Teo L W, Ho V, Ng V, Antoniadis D A and Fitzgerald E A 2002 *Appl. Phys. Lett.* **80** 2014
- [48] Hou T H, Lee C, Narayanan V, Ganguly U and Kan E C 2006 *IEEE Trans. Electron Devices* **53** 3095
- [49] Liu Z, Lee C, Narayanan V, Pei G and Kan E C 2002 *IEEE Trans. Electron Devices* **49** 1614
- [50] Wang C-C, Chiou Y-K, Chang C-H, Tseng J-Y, Wu L-J, Chen C-Y and Wu T-B 2007 *J. Phys. D: Appl. Phys.* **40** 1673
- [51] Pei Y, Yin C, Nishijima M, Kojima T, Fukushima T, Tanaka T and Koyanagi M 2009 *Appl. Phys. Lett.* **94** 063108
- [52] Mikhelashvili V, Meyler B, Yoffis S, Salzman J, Garbrecht M, Cohen-Hyams T, Kaplan W D and Eisenstein G 2009 *Appl. Phys. Lett.* **95** 023104
- [53] Panda D, Maikap S, Dhar A and Ray S K 2009 *Electrochem. Solid State Lett.* **12** H7
- [54] Maikap S, Tzeng P J, Lee H Y, Wang C C, Tien T C, Lee L S and Tsai M-J 2007 *Appl. Phys. Lett.* **91** 043114
- [55] Huang S, Banerjee S, Tung R T and Oda S 2003 *J. Appl. Phys.* **93** 576
- [56] Liu Y, Dey S, Tang S, Kelly D Q, Sarkar J and Banerjee S K 2006 *IEEE Trans. Electron Devices* **53** 2598
- [57] Ray S K, Das S, Singha R K, Manna S and Dhar A 2011 *Nanoscale Res. Lett.* **6** 224
- [58] Das S, Singha R K, Manna S, Gangopadhyay S, Dhar A and Ray S K 2011 *J Nanopart. Res.* **13** 587
- [59] Wang K L, Cha D, Liu J and Chen C 2007 *Proc. IEEE* **95** 1866
- [60] Baribeau M, Wu X, Rowell N L and Lockwood D J 2006 *J. Phys.: Condens. Matter* **18** R139
- [61] Das K and Ray S K 2010 Silicon and germanium nanocrystals for device applications in nanoclusters and nanostructured surfaces ed A K Ray (Valencia, CA: American Scientific Publishers) pp 27–77
- [62] Miller R C, Kleinman D A, Tsang W T and Gossard A C 1981 *Phys. Rev. B* **24** 1134
- [63] Cullis A G, Canham L T and Calcott P D J 1997 *J. Appl. Phys.* **82** 909
- [64] Brus L E 1986 *IEEE J. Quantum Electron.* **22** 1909
- [65] Takagahara T and Takeda K 1992 *Phys. Rev. B* **46** 15578
- [66] Garoufalidis C S, Zdetsis A D and Grimme S 2001 *Phys. Rev. Lett.* **87** 276402
- [67] Tsolakidis A and Martin R M 2005 *Phys. Rev. B* **71** 125319
- [68] Wolkin M V, Jorne J and Fauchet P M, Allan G and Delerue C 1999 *Phys. Rev. Lett.* **82** 197
- [69] Niquet Y M, Allan G, Delerue C and Lannoo M 2000 *Appl. Phys. Lett.* **77** 1182
- [70] Bulutay C 2007 *Phys. Rev. B* **76** 205321
- [71] Furukawa S and Miyasato T 1988 *Phys. Rev. B* **38** 5726
- [72] Takeoka S, Fujii M and Hayashi S 2000 *Phys. Rev. B* **62** 16820
- [73] Takeoka S, Fujii M, Hayashi S and Yamamoto K 1998 *Phys. Rev. B* **58** 7921
- [74] Kanemitsu Y, Uto H, Masumoto Y and Maeda Y 1992 *Appl. Phys. Lett.* **61** 2187
- [75] Daniel A Ruddy, Justin C Johnson, Ryan Smith E and Nathan R Neale 2010 *ACS Nano* **4** 7459
- [76] Weissker H Ch, Furthmüller J and Bechstedt F 2004 *Phys. Rev. B* **69** 115310
- [77] Leung K and Whaley K B 1997 *Phys. Rev. B* **56** 7455
- [78] Lippens E E and Lannoo M 1989 *Phys. Rev. B* **39** 935
- [79] Nicola A Hill and Whaley K B 1995 *Phys. Rev. Lett.* **75** 1130
- [80] Garcia C, Garrido B, Pellegrino P, Ferre R, Moreno J A, Morante J R, Pavesi L and Cazzanelli M 2003 *Appl. Phys. Lett.* **82** 1595
- [81] Kim S and Choi S-H 2008 *J. Korean Phys. Soc.* **52** 462
- [82] Wilson W L, Szajowski P F and Brus L E 1993 *Science* **262** 1242
- [83] Wilcoxon J P, Samara G A and Provencio P N 1999 *Phys. Rev. B* **60** 2704
- [84] Giri P K, Kesavamoorthy R, Panigrahi B K and Nair K G M 2005 *Solid State Commun.* **133** 229
- [85] Kanemitsu Y, Fukunishi Y and Kushida T 2000 *Appl. Phys. Lett.* **77** 211
- [86] Kobitski A Y, Zhuravlev K S, Wagner H P and T Zahn D R 2001 *Phys. Rev. B* **63** 115423

- [87] Takeoka S, Fujii M, Hayashi S and Yamamoto K 1999 *Appl. Phys. Lett.* **74** 1558
- [88] Julsgaard B, Balling P, Lundsgaard Hansen J, Svane A and Nylandsted Larsen A 2010 arXiv:1012.0398 [cond-mat.mes-hall]
- [89] Morisaki H, Ping F W, Ono H and Yazawa K J 1991 *Appl. Phys.* **70** 1869
- [90] Ledoux G, Gong J, Huisken F, Guillois O and Reynaud C 2002 *Appl. Phys. Lett.* **80** 4834
- [91] Shimizu-Iwayama T, Nakao S and Saitoh K 1994 *Appl. Phys. Lett.* **65** 1814
- [92] Kanazawa Y, Kageyama T, Takeoka S, Fujii M, Hayashi S and Yamamoto K 1997 *Solid State Commun.* **102** 533
- [93] Priolo F, Franzó G, Pacifici D, Vinciguerra V, Iacona F and Irrera A 2001 *J. Appl. Phys.* **89** 264
- [94] Marconi A, Anopchenko A, Wang M, Pucker G, Bellutti P and Pavesi L 2009 *Appl. Phys. Lett.* **94** 221110
- [95] Yuan Z, Anopchenko A, Daldozzo N, Guider R, Navarro-Urrios D, Pitanti A, Spano R and Pavesi L 2009 *Proc. IEEE* **97** 1250
- [96] Pavesi L and Turan R (ed) 2010 *Silicon Nanocrystals: Fundamentals, Synthesis and Applications* (Weinheim: Wiley-VCH)
- [97] Khriachtchev L (ed) 2009 *Silicon Nanophotonics: Basic Principles, Present Status and Perspectives* (Singapore: World Scientific)
- [98] Ossicini S, Pavesi L and Priolo 2003 *Light Emitting Silicon for Microphotonics* (Berlin: Springer)
- [99] Moskalenko A S, Berakdar J, Prokofiev A A and Yassievich I N 2007 *Phys. Rev. B* **76** 085427
- [100] Wang M, Huang X, Xu J, Li W, Liu Z and Kunji Chen K 1998 *Appl. Phys. Lett.* **72** 722
- [101] Liu Y *et al* 2007 *J. Appl. Phys.* **101** 104306
- [102] Jimenez-Molinos F, Gamiz F, Palma A, Cartujo P and Lopez-Villanueva J A 2002 *J. Appl. Phys.* **91** 5116
- [103] Heitmann J, Muller F, Zacharias M and Gosele U 2005 *Adv. Mater.* **17** 795
- [104] Chang S-T and Liao S-H 2009 *J. Vac. Sci. Technol. B* **27** 535
- [105] Zhang J-Y, Ye Y-H, Tan X-L and Bao X-M 2000 *Appl. Phys. A* **71** 299
- [106] Zhang J-Y, Ye Y-H and Tan X-L 1999 *Appl. Phys. Lett.* **74** 2459
- [107] Das S, Singha R K, Dhar A, Ray S K, Anopchenko A, Daldozzo N and Pavesi L 2011 *J. Appl. Phys.* **110** 024310
- [108] Das S, Manna S, Singha R K, Anopchenko A, Daldozzo N, Pavesi L, Dhar A and Ray S K 2011 *Phys. Status Solidi a* **208** 635
- [109] Fischetti M V, Neumayer D A and Cartier E A 2001 *J. Appl. Phys.* **90** 4587
- [110] Das S, Das K, Singha R K, Dhar A and Ray S K 2007 *Appl. Phys. Lett.* **91** 233118
- [111] Liu W S and Chen J S and Nicolet M -A, Arbet-Engels V and Wang K L 1992 *J. Appl. Phys.* **72** 4444
- [112] Nogami M and Abe Y 1994 *Appl. Phys. Lett.* **65** 2545
- [113] Yang H, Wang X, Shi H, Wang F, Gu X and Yao X 2002 *J. Cryst. Growth* **236** 371
- [114] Ma X, Wu F and Kauzlarich S M J 2008 *Solid State Chem.* **181** 1628
- [115] Gerion D, Zaitseva N, Saw C, Casula M F, Fakra S, Buuren T V and Galli G 2004 *Nano Lett.* **4** 597
- [116] Lu X, Ziegler K J, Ghezelbash A, Johnston K P and Korgel B A 2004 *Nano Lett.* **4** 969
- [117] Wang W, Huang J and Ren Z 2005 *Langmuir* **21** 751
- [118] Lee D C, Pietryga J M, Robel I, Werder D J, Schaller R D and Klimov V I J 2009 *Am. Chem. Soc.* **131** 3436
- [119] Chiu H W and Kauzlarich S M 2006 *Chem. Mater.* **18** 1023
- [120] Warner J H and Tilley R D 2006 *Nanotechnology* **17** 3745
- [121] Lee D C, Pietryga J M, Robel I, Werder D J, Schaller R D and Klimov V I 2009 *J. Am. Chem. Soc.* **131** 3436
- [122] Araujo L L, Julian R, Sprouster D J, Schnohr C S, Llewellyn D J, Kluth P, Cookson D J, Foran G J and Ridgway M C 2008 *Phys. Rev. B* **78** 094112
- [123] Wan Q, Lin C L, Liu W L and Wang T H 2003 *Appl. Phys. Lett.* **82** 4708
- [124] Renault O, Fourdrinier L, Martinez E, Clavelier L, Leroyer C, Barrett N and Crotti C 2007 *Appl. Phys. Lett.* **90** 052112
- [125] Das S, Singha R K, Gangopadhyay S, Dhar A and Ray S K 2010 *J. Appl. Phys.* **108** 053510
- [126] Molle A, Bhuiyan N K, Grazia T and Fanciulli M 2006 *Appl. Phys. Lett.* **89** 083504
- [127] Backman M, Djurabekova F, Pakarinen O H, Nordlund K, Araujo L L and Ridgway M C 2009 *Phys. Rev. B* **80** 144109
- [128] Yamamoto K, Hayashi S and Niwa M 2003 *Appl. Phys. Lett.* **83** 2229
- [129] Kluth P, Johannessen B, Giraud V, Cheung A, Glover C J, Azevedo G D, Foran G J and Ridgway M C 2004 *Appl. Phys. Lett.* **85** 3561
- [130] Djurabekova F and Nordlund K 2008 *Phys. Rev. B* **77** 115325
- [131] Fuchs H D, Grein C H, Thomsen C, Cardona M, Hansen W L, Haller E E and Itoh K 1991 *Phys. Rev. B* **43** 4835
- [132] Richter H, Wang Z P and Ley B 1981 *Solid State Commun.* **39** 625
- [133] Serincan U, Kartopu G, Guenes A, Finstad T G, Turan R, Ekinci Y and Bayliss S C 2004 *Semicond. Sci. Technol.* **19** 247
- [134] Jie Y X, Wee A T S, Huan C H A, Shen Z X and Choi W K 2011 *J. Appl. Phys.* **109** 033107
- [135] Sharp I D *et al* 2005 *Appl. Phys. Lett.* **86** 063107
- [136] Wellner A, Paillard V, Bonafos C, Coffin H, Claverie A, Schmidt B and Heinig K H 2003 *J. Appl. Phys.* **94** 5639
- [137] Sharp I D, Xu Q, Yi D O, Yuan C W, Beeman J W, Yu K M, Ager J W, Chrzan D C and Haller E E 2006 *J. Appl. Phys.* **100** 114317
- [138] Cerdeira F, Buchenauer C J, Fred H Pollack and Cardona M 1972 *Phys. Rev. B* **5** 580
- [139] Choi W K, Chew H G, Zheng F, Chim W K, Foo Y L and Fitzgerald E A 2006 *Appl. Phys. Lett.* **89** 113126
- [140] Ray S K and Das K 2005 *Opt. Mater.* **27** 948
- [141] Maeda Y 1995 *Phys. Rev. B* **51** 1658
- [142] Majumder S, Mondal S, Das A K and Ray S K 2009 *J. Appl. Phys.* **105** 024302
- [143] Zhang J-Y, Ye Y-H, Tan X-L and Bao X-M 1999 *J. Appl. Phys.* **86** 6139
- [144] Das S, Aluguri R, Manna S, Singha R K, Dhar A, Pavesi L and Ray S K 2012 *Nanoscale Res. Lett.* **7** 143
- [145] Chang J E *et al* 2012 *J. Phys. D: Appl. Phys.* **45** 105303
- [146] Zhang Y F, Tang Y H, Wang N, Lee C S, Bello I and Lee S T 2000 *Phys. Rev. B* **61** 4518
- [147] Okamoto S and Kanemitsu Y 1996 *Phys. Rev. B* **54** 16421
- [148] Suemoto T, Tanaka K, Nakajima A and Itakura T 1993 *Phys. Rev. Lett.* **70** 3659
- [149] Sokolov V O and Sulimov V B 1994 *Phys. Status Solidi b* **186** 185
- [150] Scott J F 1970 *Phys. Rev. B* **1** 3488
- [151] Shen J K, Wu X L, Tan C, Yuan R K and Bao X M 2002 *Phys. Lett. A* **300** 307
- [152] Kanjilal A, Rebohle L, Voelskow M, Skorupa W and Helm M 2009 *J. Appl. Phys.* **106** 026104
- [153] Lockwood D J, Lu Z H and Baribeau J M 1996 *Phys. Rev. Lett.* **76** 539
- [154] Sze S M 1981 *Physics of Semiconductor Devices* (New York: Wiley) p 497
- [155] Preziosi S, Anopchenko A, Gaburro Z, Pavesi L, Pucker G, Vanzetti L and Bellutti P 2008 *J. Appl. Phys.* **104** 063103
- [156] Lin C J and Lin G R 2005 *IEEE J. Quantum Electron.* **41** 441
- [157] Liu B *et al* 2007 *Appl. Phys. Lett.* **91** 253506
- [158] Kenyon A J 2002 *Prog. Quantum Electron.* **26** 225

- [159] Franzo G, Priolo F, Coffa S, Polman A and Carnera A 1994 *Appl. Phys. Lett.* **64** 2235
- [160] Fujii M, Yoshida M, Kanzawa Y, Hayashi S and Yamamoto K 1997 *Appl. Phys. Lett.* **71** 198
- [161] Franzó G, Pacifici D, Vinciguerra V, Priolo F and Iacona F 2000 *Appl. Phys. Lett.* **76** 2167
- [162] Savchyn O, Kik P G, Todi R M and Coffey K R 2008 *Phys. Rev. B* **77** 10980121
- [163] Nazarov A, Sun J M, Skorupa W, Yankov R A, Osuyuk I N, Tjagulskii I P, Lysenko V S and Gebel T 2005 *Appl. Phys. Lett.* **86** 151914
- [164] Seo S-Y and Shin J H 2004 *Appl. Phys. Lett.* **84** 4379
- [165] Li D, Zhang X, Jin L and Yang D 2010 *Opt. Express* **18** 27191
- [166] Ennen H, Schneider J, Pomrenke G and Axmann A 1983 *Appl. Phys. Lett.* **43** 943
- [167] Palm J, Gan F, Zheng B, Michel J and Kimerling L C 1996 *Phys. Rev. B* **54** 17603
- [168] Izeddin I, Timmerman D, Gregorkiewicz T, Moskalenko A S, Prokofiev A A, Yassievich I N and Fujii M 2008 *Phys. Rev. B* **78** 035327
- [169] Fujii M, Yoshida M, Kanzawa Y, Hayashi S and Keiichi Y 1997 *Appl. Phys. Lett.* **71** 1198
- [170] Heinrich J L, Curtis C J, Credo G M, Kavanagh K L and Sailor M J 1992 *Science* **255** 66
- [171] Pavesi L, Dal Negro L, Mazzoleni C, Franzó G and Priolo F 2000 *Nature* **408** 440
- [172] Ossicini S, Arcangeli C, Bisi O, Degoli E, Luppi M, Magri R, Negro L D and Pavesi L 2003 Gain theory and models in silicon nanostructures *Towards the First Silicon Laser* ed L Pavesi *et al* (*Nato Science Series* vol 93) (Dordrecht: Kluwer) pp 261–280
- [173] Khriachtchev L, Rasanen M, Novikov S and Sinkkonen J 2001 *Appl. Phys. Lett.* **79** 1249
- [174] Nayfeh M H, Barry N, Therrien J, Akcakir O, Gratton E and Belomoin G 2001 *Appl. Phys. Lett.* **78** 1131
- [175] Yerci S, Li R and Dal Negro L 2010 *Appl. Phys. Lett.* **97** 081109
- [176] Han H S, Seo S Y and Shin J H 2001 *Appl. Phys. Lett.* **79** 4568
- [177] Kik P G, Brongersma M L and Polman A 2000 *Appl. Phys. Lett.* **76** 2325
- [178] Savchyn O, Ruhge F R, Kik P G, Todi R M, Coffey K R, Nukala H and Heinrich H 2007 *Phys. Rev. B* **76** 195419
- [179] Förster T 1948 *Ann. Phys.* **2** 55
- [180] Khriachtchev L (ed) 2009 *Silicon Nanophotonics: Basic Principles, Present Status and Perspectives* (Singapore: World Scientific Publishing)
- [181] Pacifici D, Franzó G, Priolo F, Iacona F and Dal Negro L 2003 *Phys. Rev. B* **67** 245301
- [182] Garrido B, Garcia C, Seo S-Y, Pellegrino P, Navarro-Urrios D, Daldosso N, Pavesi L, Gourbilleau F and Rizk R 2007 *Phys. Rev. B* **76** 245308
- [183] Franzó G, Pacifici D, Vinciguerra V, Priolo F and Iacona F 2000 *Appl. Phys. Lett.* **76** 2167
- [184] Ennen H, Pomrenke G, Axmann A, Eisele K, Haydl W and Schneider J 1985 *Appl. Phys. Lett.* **46** 381
- [185] Iacona F, Pacifici D, Irrera A, Miritello M, Franzo G, Priolo F, Sanfilippo D, Di Stefano G and Fallica P G 2002 *Appl. Phys. Lett.* **81** 3242
- [186] Jambois O, Gourbilleau F, Kenyon A, Montserrat J, Rizk R and Garrido B 2010 *Opt. Express* **18** 2230
- [187] Muscara A, Castagna M E, Leonardi S and Coffa S 2011 *IEEE J. Quantum Electron.* **47** 1362
- [188] Priolo F, Presti C D, Franzo G, Irrera A, Crupi I, Iacona F, Di Stefano G, Piana A, Sanfilippo D and Fallica P G 2006 *Phys. Rev. B* **73** 113302
- [189] Miller G M, Briggs R M and Atwater H A 2010 *J. Appl. Phys.* **108** 063109
- [190] Anopchenko A *et al* 2012 *J. Appl. Phys.* **111** 063102
- [191] Daldosso N and Pavesi L 2009 *Laser Photon. Rev.* **3** 508
- [192] Sato S, Nozaki S and Morisaki H 1995 *Appl. Phys. Lett.* **66** 3176
- [193] Franzò G, Vinciguerra V and Priolo F 1999 *Appl. Phys.* **69** 3
- [194] Kenyon A J 2003 *Curr. Opin. Solid State Mater. Sci.* **7** 143
- [195] Jensen J S, Pedersen T P L, Chevallier J, Nielsen B B and Larsen A N 2006 *Nanotechnology* **17** 2621
- [196] Chen J H, Pang D, Cheong H M, Wickboldt P and Paul W 1995 *Appl. Phys. Lett.* **67** 2182
- [197] Heng C L, Finstad T G, Storås P, Li Y J, Gunnæs A E and Nilsen O 2004 *Appl. Phys. Lett.* **85** 4475
- [198] Yu K M, Beeman J W, Watanabe M, Ager J W III, Chrzan D C and Haller E E 2009 *Appl. Phys. Lett.* **95** 201904
- [199] Aluguri R, Das S, Manna S, Singha R K and Ray S K 2012 *Opt. Mater.* **34** 1430
- [200] Kanjilal A, Rebole L, Voelskow M, Skorupa W and Helm M 2009 *Appl. Phys. Lett.* **94** 051903
- [201] van den Hoven G N, van der Elsken J A, Polman A, van Dam C, van Uffelen K W M and Smit M K 1997 *Appl. Opt.* **36** 3338
- [202] van den Hoven G N, Koper R J I M, Polman A, van Dam C, van Uffelen K W M and Smit M K 1996 *Appl. Phys. Lett.* **68** 1886
- [203] Almeida R M, Vasconcelos H C, Gonçalves M C and Santos L F 1998 *J. Non-Cryst. Solids* **232** 65
- [204] Auzel F and Goldner P 2001 *Opt. Mater.* **16** 93
- [205] Guha S and Bojarczuk N A 1998 *Appl. Phys. Lett.* **72** 415
- [206] Fang A W, Park H, Cohen O, Jones R, Paniccia M J and Bowers J E 2006 *Opt. Express* **14** 9203
- [207] Liang D and Bowers J E 2008 *J. Vac. Sci. Technol. B* **26** 1560
- [208] Liang D, Fiorentino M, Okumura T, Chang H-H, Spencer D T, Kuo Y-H, Fang A W, Dai D, Beausoleil R G and Bowers J E 2009 *Opt. Express* **17** 20355
- [209] Justice J, Bower C, Meitl M, Mooney M B, Gubbins M A and Corbett B 2012 *Nature Photon.* **6** 610
- [210] Duan G H, Fedeli J M, Keyvaninia S and Thomson D 2012 *European Conf. and Exhibition on Optical Communications (Amsterdam)* (Washington DC: Optical Society of America) Tu.4.E.2
- [211] Green M A, Zhao J, Wang A, Reece P J and Gal M 2001 *Nature* **412** 805
- [212] Gelloz B and Koshida N 2000 *J. Appl. Phys.* **88** 4319
- [213] Cheng C-H, Lien Y-C, Wu C L and Lin G-R 2013 *Opt. Express* **21** 391
- [214] Kahng D and Sze S M 1967 *Bell Syst. Tech. J.* **46** 1288
- [215] Shi Y, Saito K, Ishikuro H and Hiramoto T 1998 *J. Appl. Phys.* **84** 2358
- [216] <http://investors.micron.com/releasedetail.cfm?ReleaseID=467770>
- [217] www.freescale.com/files/32bit/doc/.../BRKINETISELS.pdf
- [218] Gay G *et al* 2012 *IEEE Trans. Electron Devices* **59** 4
- [219] She M 2003 *PhD Dissertation* University of California, Berkeley
- [220] Maikap S, Lee H Y, Wang T Y, Tzeng P J, Wang C C, Lee L S, Liu K C, Yang J R and Tsai M J 2007 *Semicond. Sci. Technol.* **22** 884
- [221] Ostraat M L, De Blauwe J W, Green M L, Bell L D, Brongersma M L, Casperson J, Flagan R C and Atwater H A 2001 *Appl. Phys. Lett.* **79** 433
- [222] Tiwari S, Wahl J A, Silva H, Rana F and Welser J J 2000 *Appl. Phys. A* **71** 403
- [223] Ohba R, Sugiyama N, Uchida K, Koga J and Toriumi A 2002 *IEEE Trans. Electron Devices* **49** 1392
- [224] Chung S S, Tseng Y H, Huang Y H, Lai C S, Hsu Y Y, Eric H, Terry C, Peng L C and Chu C H 2007 *IEDM* p 457
- [225] Masarotto L, Molas G, Jalaguier E, Gay G, Colonna J P, Hartmann J M and Yckache K 2011 *Semicond. Sci. Technol.* **26** 025008

- [226] Depas M, Vermeire B, Mertens P W, Vanmeirhaeghe R L and Heyns M M 1995 *Solid-State Electron.* **38** 1465
- [227] Jiang D *et al* 2011 *Semicond. Sci. Technol.* **26** 115008
- [228] Rao R A *et al* 2005 *Solid-State Electron.* **49** 1722
- [229] Zhou X, Usami K, Rafiq M A, Tsuchiya Y, Mizuta H and Oda S 2008 *J. Appl. Phys.* **104** 024518
- [230] Banerjee S, Huang S and Oda S 2003 *IEEE Trans. Nanotechnol.* **2** 2
- [231] King Y C, King T J and Hu C 1998 *Technical Digest Int. Electron Devices Meeting* p 115
- [232] King Y C, King T J and Hu C 2001 *IEEE Trans. Electron Devices* **48** 696
- [233] Kanjilal A, Lundsgaard J, Gaiduk P H, Cherkashin N L N A, Claverie A, Normand P, Kapelanakis E, Skarlatos D and Tsoukalas D 2003 *Appl. Phys. Lett.* **82** 1212
- [234] Aluguri R, Das S, Singha R K and Ray S K 2012 *Curr. Appl. Phys.* **13** 12
- [235] Li B, Liu J, Liu G F and Yarmoff J A 2007 *Appl. Phys. Lett.* **91** 132107
- [236] Winkenwerder W, Yueran L, Ferrer D, Shahrjerdi D, Stanley S K, Ekerdt J G and Banerjee S K 2008 *IEEE Trans. Electron Devices* **55** 3610
- [237] Kanoun M, Souifi A, Baron T and Mazen F 2004 *Appl. Phys. Lett.* **84** 5079
- [238] Park C J, Cho K H, Yang W C, Cho H Y and Choi S H 2006 *Appl. Phys. Lett.* **88** 071916
- [239] Chen W R, Chang T C, Hsieh Y T and Chang C Y 2009 *IEEE Trans. Nanotechnol.* **8** 185
- [240] Peibst R, Frenburg M, Bugiel E and Hofmann K R 2010 *J. Appl. Phys.* **108** 054316
- [241] Das K, Maikap S, Dhar A, Mathur B K and Ray S K 2003 *Electron. Lett.* **39** 1865
- [242] Wan Q, Lin C L, Liu W L and Wang T H 2003 *Appl. Phys. Lett.* **82** 4708
- [243] Baron T, Pelissier B, Perniola L, Mazen F, Hartmann J M and Rolland G 2003 *Appl. Phys. Lett.* **83** 1444
- [244] Beenakker C W 1991 *Phys. Rev. B* **44** 1646
- [245] Gusev E P *et al* 2001 *Technical Digest of IEDM* p 451
- [246] Kim D W, Kim T and Banerjee S K 2003 *IEEE Trans. Electron Devices* **50** 1823
- [247] Wang Y Q, Chen J H, Yoo W J, Yeo Y C, Kim S J, Gupta R, Tan Z Y L, Kwong D L, Du A Y and Balasubramannia N 2004 *Appl. Phys. Lett.* **84** 5407
- [248] Lee S J, Luan H F, Bai W P, Lee C H, Jeon T S, Senzaki Y, Roberts D and Kwong D L 2000 *IEDM Technical Digest* p 31
- [249] Zhu W J, Ma T P, Tamagawa T, Kim J and Di Y 2002 *IEEE Electron Device Lett.* **23** 97
- [250] Winkler O, Merget F, Heuser M, Hadam B, Baus M, Spangenberg B and Kurz H 2002 *Microelectron. Eng.* **61** 497
- [251] Kim J K, Cheong H J, Kim Y, Yi J Y and Park H J 2003 *Appl. Phys. Lett.* **82** 2527
- [252] Baik S *et al* 2003 *IEDM Technical Digest* p 545
- [253] Govoreanu B, Blomme P, Rosmeulen M, Van Houdt J and De Meyer K 2003 *IEEE Electron Device Lett.* **24** 99101
- [254] Caspelson J D, Bell L D and Atwater H A 2002 *J. Appl. Phys.* **92** 261
- [255] Zhang G, Ra C H, Li H M, Yang C and Yoo W J 2009 *Technical Digest—Int. Electron Devices Meeting* p 835
- [256] Lee C, Ganguly U, Narayanan V, Hou T H, Kim J and Kan E C 2005 *IEEE Electron Device Lett.* **26** 879
- [257] Singh P K, Bisht G, Auluck K, Sivatheja M, Hofmann R, Singh K K and Mahapatra S 2010 *IEEE Trans. Electron Devices* **57** 1829
- [258] Lee C, Meteer J, Narayanan V and Kan E C 2005 *J. Electron. Mater.* **34** 1
- [259] Kapetanakis E, Normand P, Tsoukalas D, Beltsios K, Stoemenos J, Zhang S and Berg J 2000 *Appl. Phys. Lett.* **77** 3450
- [260] Chen C H, Chang T C, Liao I H, Xi P B, Hsieh J, Jason C, Huang T, Sze S M, Chen U S and Chen J R 2008 *Appl. Phys. Lett.* **92** 013114
- [261] Chang T C, Jian F Y, Chen S C and Tsai Y T 2011 *Mater. Today* **14** 608
- [262] Maikap S, Wang T Y, Tzeng P J, Lin C H, Lee L S, Yang J R and Tsai M J 2007 *Appl. Phys. Lett.* **90** 253108
- [263] Liu Y, Chen T P, Ding L, Wong J I, Yang M, Liu Z, Li Y B and Zhang S, 2010 *J. Nanosci. Nanotechnol.* **10** 599
- [264] Wang Q *et al* 2008 *J. Phys. D: Appl. Phys.* **41** 035109
- [265] Kim H, Woo S, Kim H, Bang S, Kim Y, Choi D and Jeon H 2009 *Electrochem. Solid-State Lett.* **12** H92
- [266] Ren J, Li B, Zheng J G and Liu J 2012 *Solid-State Electron.* **67** 23
- [267] Zhang M, Chen W, Ding S J, Liu Z Y, Huang Y, Liao Z W and Zhang D W 2008 *J. Phys. D: Appl. Phys.* **41** 032007
- [268] Maikap S, Banerjee W, Tien T C, Wang T Y and Yang J R 2011 *J. Nanomaterials* **2011** 810879
- [269] Lin C H and Kuo Y 2011 *J. Appl. Phys.* **110** 024101
- [270] Choi S *et al* 2007 *J. Phys. D: Appl. Phys.* **40** 142
- [271] Banerjee W, Maikap S, Tien T C, Li W C and Yang J R 2011 *J. Appl. Phys.* **110** 074309
- [272] Lee J J and Kwong D L 2005 *IEEE Trans. Electron Devices* **52** 507
- [273] Ryu S W, Mo C B, Hong S H and Choi Y K 2008 *IEEE Trans. Nanotechnol.* **7** 14
- [274] Ryu S W, Lee J W, Han J W, Kim S and Choi Y K 2009 *IEEE Trans. Electron Devices* **56** 377
- [275] Wu Y H, Chen L L, Lin Y S, Chang C H, Huang J H and Yu G P 2009 *IEEE Electron Device Lett.* **30** 617
- [276] Lim S H 2005 *Symp. VLSI Technical Digest* p 190
- [277] Zhou H, Li B, Yang Z, Zhan N, Yan D, Lake R K and Liu J 2011 *IEEE Trans. Nanotechnol.* **10** 499
- [278] Lee J-S, Kim Y-M, Kwon J-H, Shin H, Sohn B-Y and Lee J 2009 *Adv. Mater.* **21** 178
- [279] Maikap S, Rahaman S Z and Tien T C 2008 *Nanotechnology* **19** 435202
- [280] Maikap S, Tzeng P J, Wang T Y, Lin C H, Lee L S, Yang J R and Tsai M J 2008 *Electrochem. and Solid State Lett.* **11** K50
- [281] Maikap S, Wang T Y, Tzeng P J, Lin C H, Tien T C, Lee L S, Yang J R and Tsai M J 2007 *Appl. Phys. Lett.* **90** 262901